

# Fundamental parameters for double-lined spectroscopic and detached eclipsing binary system J064726.39+223431.6.

Mikhail Kovalev,<sup>1,2,3,4</sup>★ Song Wang,<sup>5</sup> Xuefei Chen<sup>1,2,6</sup> and Zhanwen Han<sup>1,2,6</sup>

<sup>1</sup>Yunnan Observatories, China Academy of Sciences, Kunming 650216, China

<sup>2</sup>Key Laboratory for the Structure and Evolution of Celestial Objects, Chinese Academy of Sciences, Kunming 650011, China

<sup>3</sup>Sternberg Astronomical Institute, M. V. Lomonosov Moscow State University, Leninskie Gory, Moscow 119991, Russia

<sup>4</sup>Key Laboratory of Optical Astronomy, National Astronomical Observatories, Chinese Academy of Sciences, Beijing 100101, China

<sup>5</sup>Center for Astronomical Mega-Science, Chinese Academy of Sciences, 20A Datun Road, Chaoyang District, Beijing 100012, China

Accepted XXX. Received YYY; in original form ZZZ

## ABSTRACT

We present a study of the detached eclipsing binary J064726.39+223431.6 using spectra from the LAMOST medium-resolution spectra and TESS photometry. We use full-spectrum fitting to derive radial velocities and spectral parameters:  $T_{\text{eff},A,B} = 6177, 5820$  K,  $V \sin i_{A,B} = 59, 50$  km s<sup>-1</sup> and  $[\text{Fe}/\text{H}]_{A,B} = -0.19$  dex. The orbital solution and light curve analysis suggest that it is a close pair of fast rotating stars on a circular orbit. We measure their masses to be  $M_{A,B} = 1.307 \pm 0.007, 1.129 \pm 0.005 M_{\odot}$  and their radii to be  $R_{A,B} = 1.405 \pm 0.052, 1.219 \pm 0.060 R_{\odot}$  resulting in surface gravities of  $\log(g)_{A,B} = 4.259 \pm 0.033, 4.319 \pm 0.042$  (cgs). Theoretical models cannot match all of these properties, predicting significantly higher  $T_{\text{eff}}$  for a given metallicity. The derived age of the system is 1.56 Gyr, which indicates that both components are younger than Sun, which contradicts to much longer orbit’s circularisation timescale.

**Key words:** stars : fundamental parameters – binaries : spectroscopic – stars individual: J064726.39+223431.6

## 1 INTRODUCTION

Binary stellar systems are very important objects for astronomy, since they allow us to learn more than from single stars. For example, observations of the periodic eclipses and changes in line-of-sight velocities (RV) can be used to directly measure sizes and masses of the stellar components, if orbital inclination is high enough. Such dynamical measurements in detached eclipsing binaries (dEBs) minimally rely on stellar models (Andersen 1991; Torres et al. 2010), compared to other methods such as “gravity mass” (estimated from parallax, extinction, magnitude, effective temperature, and surface gravity) or “evolutionary mass” (derived from theoretical isochrones with the effective temperature, surface gravity, and metallicity as input).

The well-known catalogue DEBCat includes more than 300 dEB systems with dynamical mass and radius measurements to the 2% precision (Southworth 2015). Recently, by using the LAMOST (Large Sky Area Multi-Object fiber Spectroscopic Telescope, also known as Guoshoujing telescope) medium-resolution spectral (MRS) data and other time-domain photometric data, Xiong et al. (2022) derived independent atmospheric parameters and accurate masses and radii for 56 new dEBs. These measurements with high

precision can be used to study the correlations of different physical parameters (e.g., the mass-luminosity, mass-radius, and mass-effective temperature relations) and provide useful constraints on theoretical models of stellar evolution (Torres et al. 2010; Eker et al. 2015, 2018; Han et al. 2020).

More than 2400 double-lined spectroscopic binaries (SB2) were identified in Kovalev et al. (2022b) based on the LAMOST-MRS survey (Liu et al. 2020) and we selected one previously known dEB star ZTF J064726.39+223431.6 with large RV semiamplitude, based on Wang et al. (2021), to estimate physical parameters for both components in this system. This SB2 is also contained by the new “High-precision Empirical Stellar Mass Library” constructed by Xiong et al. (2022). Table 1 list the designations of this system in literature.

In this paper we use the LAMOST-MRS data and additional photometric data to measure physical parameters for both stars in this system and test our approach of multiple-epoch SB2 fitting, developed in Kovalev et al. (2022a). The paper is organised as follows: in Sections 2 and 3 we describe the observations and methods. Section 4 presents our results. In Section 5 we discuss the results in context of binary system evolution. In Section 6 we summarise the paper and draw conclusions.

★ E-mail: mikhail.kovalev@ynao.ac.cn

**Table 1.** Designations from the literature: a–[Gaia Collaboration et al. \(2022\)](#), b–[Watson et al. \(2006\)](#), c–[Stassun et al. \(2019\)](#), d–[Jayasinghe et al. \(2018\)](#), e–[Chen et al. \(2020\)](#), f–[Qian et al. \(2019\)](#).

Property	Value	Reference
Gaia DR3	3378682653860701568	a
Variable Star indeX	167003	b
TESS input catalogue	TIC57046871	c
ASAS-SN	J064726.41+223431.7	d
ZTF	J064726.39+223431.6	e
LAMOST	J064726.39+223431.7	f

## 2 OBSERVATIONS

### 2.1 Spectra

LAMOST is a 4-meter quasi-meridian reflective Schmidt telescope with 4000 fibers installed on its 5-degree-FoV focal plane. These configurations allow it to observe spectra for at most 4000 celestial objects simultaneously ([Cui et al. \(2012\)](#); [Zhao et al. \(2012\)](#)). All available spectra were downloaded from [www.lamost.org](http://www.lamost.org) under the designation J064726.39+223431.7. We use the spectra taken at a resolving power of  $R = \lambda/\Delta\lambda \sim 7500$ . Each spectrum is divided into two arms: blue from 4950 Å to 5350 Å and red from 6300 Å to 6800 Å. We convert the heliocentric wavelength scale in the observed spectra from vacuum to air using PyAstronomy ([Czesla et al. 2019](#)). Observations are carried out from 2019-11-19 till 2021-02-19, covering 16 nights with time base of 480 days. Since the period is short ( $P = 1.217$  d  $\sim$  29 hrs) we analysed spectra taken during short 20 minutes exposures, unlike [Kovalev et al. \(2022a\)](#) and [Kovalev et al. \(2022b\)](#), where spectra stacked for the whole night were used. We discarded all spectra taken on three nights with MJD=58829, 59216, 59249 d due to excess noise. In total we have 72 spectra, where the average signal-to-noise ratio (S/N) of a spectrum ranges from 16 to 54  $\text{pix}^{-1}$  and the majority of the spectra have S/N around 40  $\text{pix}^{-1}$ .

### 2.2 Photometry

We have downloaded publicly available ZTF light curves (LC)<sup>1</sup>. These LCs contain 1444 datapoints in  $r$  band and 370 datapoints in  $g$  bands and cover timebase 1240 d and 1125 d respectively. We also download LC in  $V$  band from the ASSAS-SN portal<sup>2</sup>. It contains only 183 datapoints and covers timebase 1212 d. After phase-folding of these LCs with the period we found that only ZTF LC from the  $r$  band has good coverage of eclipses, therefore we use only it in the further analysis.

The Transiting Exoplanet Survey Satellite (TESS [Ricker et al. 2015](#)) mission observed this star in two sectors 44 and 45, which covers  $\sim 27$  days each. The LCs are not available on the MAST<sup>3</sup> portal yet, therefore we use eleanor ([Feinstein et al. 2019](#); [Brasseur et al. 2019](#)) to extract the LC datasets. We use default settings and clip the edges of the LC, as they have some processing artifacts, see Figure 1. After the clipping, LCs contain 2953 and 3160 datapoints for sectors 44 and 45, respectively, and have relative (non-calibrated)

<sup>1</sup> [https://irsa.ipac.caltech.edu/cgi-bin/ZTF/nph\\_light\\_curves](https://irsa.ipac.caltech.edu/cgi-bin/ZTF/nph_light_curves)

<sup>2</sup> <https://asas-sn.osu.edu/variables/AP24824756>

<sup>3</sup> <https://mast.stsci.edu/portal/Mashup/Clients/Mast/Portal.html>

stellar magnitudes. The background subtraction is not optimal for these datasets, therefore we analyse them separately.

## 3 METHODS

### 3.1 Spectral fitting

Our spectroscopic analysis includes two consecutive stages:

(i) analysis of individual observations by binary and single-star spectral models, where we normalise the spectra and make a rough estimation of the spectral parameters, see brief description in Section 3.1.1.

(ii) simultaneous fitting of multiple-epochs with a binary spectral model, using constraints from binary dynamics and values from the previous stage as an input, see Section 3.1.2.

A LAMOST-MRS implementation of this method was first presented in [Kovalev et al. \(2022a\)](#).

#### 3.1.1 Individual spectra.

The single-star spectral model is described in Appendix A. The normalised binary model spectrum is generated as a sum of the two Doppler-shifted, normalised single-star model spectra  $f_{\lambda,i}$  scaled according to the difference in luminosity, which is a function of the  $T_{\text{eff}}$  and stellar size. We assume both components to be spherical and use following equation:

$$f_{\lambda,\text{binary}} = \frac{f_{\lambda,2} + k_{\lambda}f_{\lambda,1}}{1 + k_{\lambda}}, \quad k_{\lambda} = \frac{B_{\lambda}(T_{\text{eff},1}) M_1}{B_{\lambda}(T_{\text{eff},2}) M_2} 10^{\log(g)_2 - \log(g)_1} \quad (1)$$

where  $k_{\lambda}$  is the luminosity ratio per wavelength unit,  $B_{\lambda}$  is the blackbody radiation (Planck function),  $T_{\text{eff}}$  is the effective temperature,  $\log(g)$  is the surface gravity and  $M$  is the mass. Throughout the paper we always assume the primary star to be brighter.

The binary model spectrum is later multiplied by the normalisation function, which is a linear combination of the first four Chebyshev polynomials (similar to [Kovalev et al. 2019](#)), defined separately for blue and red arms of the spectrum. The resulting spectrum is compared with the observed one using the `scipy.optimize.curve_fit` function, which provides optimal spectral parameters, radial velocities (RV) of each component plus the mass ratio and two sets of four coefficients of Chebyshev polynomials. We keep metallicity equal for both components. In total we have 18 free parameters for a binary fit. We estimate goodness of the fit parameter by reduced  $\chi^2$ :

$$\chi^2 = \frac{1}{N-18} \sum [(f_{\lambda,\text{observed}} - f_{\lambda,\text{model}}) / \sigma_{\lambda}]^2 \quad (2)$$

where  $N$  is a number of wavelength points in the observed spectrum. To explore the whole parameter space and to avoid local minima we run the optimisation six times with different initial parameters of the optimiser. We select the solution with minimal  $\chi^2$  as a final result.

Additionally, every spectrum is analysed by a single star model, which is identical to a binary model when both components have all equal parameters, so we fit only for 13 free parameters. Using this single star solution we compute the difference in reduced  $\chi^2$  between two solutions and the improvement factor, computed using Equation 3 similar to [El-Badry et al. \(2018\)](#). This improvement

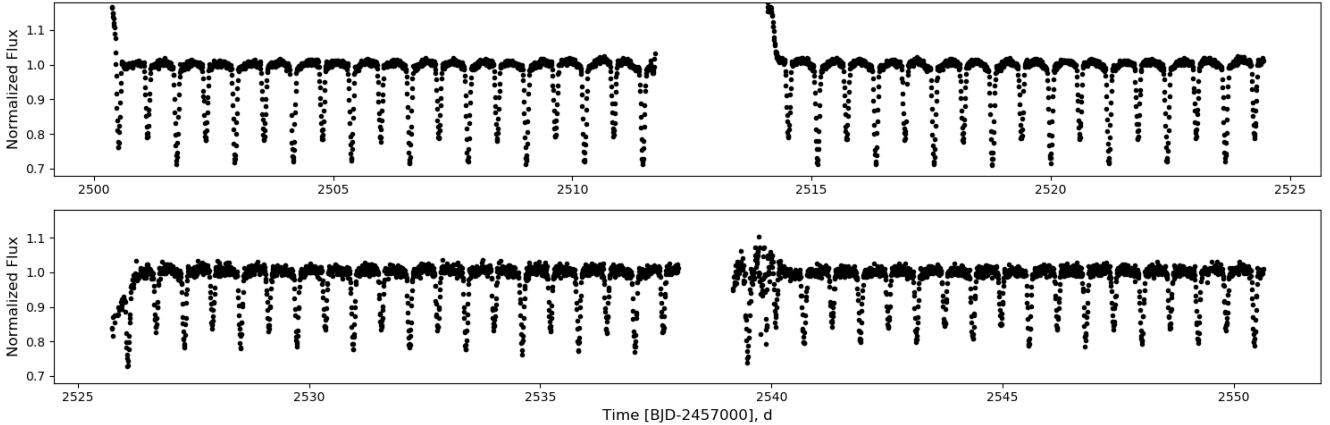


**Figure 1.** Light curves extracted by eleanor from TESS sectors 44 (top) and 45 (bottom).

factor estimates the absolute value the difference between the two fits and weights it by difference between two solutions.

$$f_{\text{imp}} = \frac{\sum \left[ \left( |f_{\lambda, \text{single}} - f_{\lambda}| - |f_{\lambda, \text{binary}} - f_{\lambda}| \right) / \sigma_{\lambda} \right]}{\sum \left[ |f_{\lambda, \text{single}} - f_{\lambda, \text{binary}}| / \sigma_{\lambda} \right]}, \quad (3)$$

where  $f_{\lambda}$  and  $\sigma_{\lambda}$  are the observed flux and corresponding uncertainty,  $f_{\lambda, \text{single}}$  and  $f_{\lambda, \text{binary}}$  are the best-fit single-star and binary model spectra, and the sum is over all wavelength pixels.

### 3.1.2 Multiple-epochs fitting.

We explore the results from the fitting of the individual epochs and find that a result's quality clearly depends on separation of RVs. Clear double-lined spectra show that spectral lines are significantly broadened ( $V \sin i \sim 60 \text{ km s}^{-1}$ ), thus at phases near the conjunctions our fitting algorithm often cannot reliably separate primary/secondary contributions. Fortunately we can automatically separate good results with clear double-lines using  $f_{\text{imp}}$ . Thus we decided to use only five individual spectra with highest  $f_{\text{imp}}$  in multiple-epoch fitting.

If two components in our binary system are gravitationally bound, their radial velocities should agree with the following equation:

$$\text{RV}_A = \gamma_{\text{dyn}}(1 + q_{\text{dyn}}) - q_{\text{dyn}}\text{RV}_B, \quad (4)$$

where  $q_{\text{dyn}} = M_B/M_A$  - mass ratio of binary components and  $\gamma_{\text{dyn}}$  - systemic velocity. Using this equation we can directly measure the systemic velocity and mass ratio.

To reduce the number of free parameters in the multiple-epochs fitting we use only  $\text{RV}_A$  and computed  $\text{RV}_B$  using Equation 4. The same value of mass ratio is used in Equation 1. Unlike the previous stage, we fit  $[\text{Fe}/\text{H}]$  for both components. In total we fit for 15 free parameters. We fit five previously normalised individual epoch's spectra with maximal improvement factor, using their binary spectral parameters values for initialisation. We select the solution with minimal  $\chi^2$  as a final result.

### 3.1.3 Typical errors estimation

We estimate the typical errors of the multiple-epochs fitting by testing it's performance on the dataset of synthetic binaries. We

generated 3000 mock binaries using uniformly distributed mass-ratios from 0.7 to 1.0,  $T_{\text{eff}}$  from 4600 to 8400 K,  $\log(g)$  from 2.6 to 4.6 (cgs) and  $V \sin i$  from 1 to 100  $\text{km s}^{-1}$ . Metallicity was set to  $[\text{Fe}/\text{H}] = 0.0$  dex in both components. For each star, we computed 5 mock binary spectra using radial velocities computed for circular orbits with the semiamplitude of the primary component 20  $\text{km s}^{-1}$  at randomly chosen phases. These models were degraded by Gaussian noise according to  $S/N = 100 \text{ pix}^{-1}$ . We performed exactly the same analysis on this simulated dataset as we did for the observations. We checked how well the mass ratio and the spectral parameters of the primary and secondary components can be recovered by calculating the average and standard deviation of the residuals. For the primary components we have  $\Delta T_{\text{eff}} = 95 \pm 239 \text{ K}$ ,  $\Delta \log(g) = 0.07 \pm 0.14$  cgs units,  $\Delta V \sin i = -1 \pm 12 \text{ km s}^{-1}$  and  $\Delta[\text{Fe}/\text{H}] = -0.02 \pm 0.08$  dex. For the secondary components we have  $\Delta T_{\text{eff}} = 35 \pm 364 \text{ K}$ ,  $\Delta \log(g) = 0.05 \pm 0.21$  cgs units,  $\Delta V \sin i = -3 \pm 21 \text{ km s}^{-1}$  and  $\Delta[\text{Fe}/\text{H}] = 0.04 \pm 0.18$  dex. The mass ratio recovery has  $\Delta q = 0.05 \pm 0.15$ .

## 3.2 Orbital fitting

To get the orbital solution, we select 55 RVs of the primary component separated by at least 60  $\text{km s}^{-1}$  from the systemic velocity  $\gamma$ . RVs close to  $\gamma$  can be affected by the Rossiter-McLaughlin (RM) effect (Rossiter 1924; McLaughlin 1924), as several spectra were possibly taken during eclipses, thus we don't use them in orbital fitting. We collect all RV measurements in Table B1

In the next step, selected  $\text{RV}_A$  are used to fit circular orbits using generalised Lomb-Scargle periodogram (GLS) code by Zechmeister & Kürster (2009) :

$$\text{RV}_A(t) = \gamma - K_A \sin \left( \frac{2\pi}{P} (t - t_0) \right), \quad (5)$$

where  $\gamma$  - is the systemic velocity,  $P$  - is the period,  $t_0$  - is the conjunction time,  $K$  - is the radial velocity semiamplitude. We also fit to a Keplerian orbit and find that the eccentricity is equal to zero, so a circular orbit is a valid assumption.

**Table 2.** GLS orbital solution.

Parameter	Value
$P$ , d	$1.217770 \pm 0.000003$
$t_0$ , HJD d	$2458808.8088 \pm 0.0003$
$K_A$ , km s <sup>-1</sup>	$122.80 \pm 0.23$
$\gamma_A$ , km s <sup>-1</sup>	$-16.98 \pm 0.16$

### 3.3 Light curve fitting

We used the JKTEBOP code (version 40)<sup>4</sup> by Southworth (2013) to simultaneously fit the LC and RV timeseries. We used only ZTF  $r$  band and TESS datasets, because of their better coverage of the eclipses. Unlike GLS, JKTEBOP allows us to fit RVs measured for both components. Our fitting was initialised using  $P, t_0, \gamma$  values from the GLS fit. We used tables of the limb and gravity darkening coefficients from Claret & Bloemen (2011) and Claret (2017), and linearly interpolated them for spectral parameters from multiple-epochs fits. We used four-parameter limb darkening coefficients  $c_i, i = 1, 4$ . We took into account a useful comment by Torres (2021) on the usage of gravity darkening coefficients in JKTEBOP.

The systemic velocity was fitted for both binary components. Additionally, we fit for a “third” light contribution  $L_3$  and the nuisance parameter the out-of-eclipse magnitude  $S_0$  for all three datasets. In total we fit for 16 parameters:  $J$  the central surface brightness ratio,  $(R_A + R_B)/a$  the ratio of the sum of stellar radii to the semimajor axis,  $R_B/R_A$  the ratio of the radii,  $i$  the inclination,  $e \cos \omega, e \sin \omega$  the eccentricity multiplied by the cosine and sine of the periastron longitude, reflected light  $A_{A,B}$ ,  $P$  the period,  $t_0$ , semi-amplitudes and systemic velocities  $K_{A,B}, \gamma_{A,B}, L_3$  and  $S_0$ . We use integration ring size  $5^\circ$  for the ZTF  $r$  and  $1^\circ$  for the TESS LCs.

At first we run the JKTEBOP code in the mode “Task 4” to discard outliers larger than three sigma and allow it adjusting observational errors through several iterations until reduced  $\chi^2$  reaches unity. This removes 24, 17, 13 datapoints from ZTF  $r$ , TESS 44, 45 LC datasets, respectively and keeps all 110 RV datapoints. Then we run JKTEBOP in the residual permutation (RP) mode (Task 9 - “red” noise) to estimate uncertainties using 1417, 2935 and 3147 residual-shifted fits for ZTF  $r$  and TESS 44, 45 datasets respectively, similarly to Southworth et al. (2011); Southworth (2013).

## 4 RESULTS

In the Figure 2 we show the best fit by multiple-epochs binary model for an epoch with large RV separation. We zoom into the wavelength range around the magnesium triplet and H $\alpha$  and in a 70 Å interval in the red arm, where many double lines are clearly visible. Both components are on main sequence, where the primary star ( $T_{\text{eff}} = 6104$  K,  $\log(g) = 3.86$  cgs,  $[\text{Fe}/\text{H}] = -0.29$  dex,  $V \sin i = 58$  km s<sup>-1</sup>) contributes around 70% in the visible light, while the secondary star ( $T_{\text{eff}} = 5980$  K,  $\log(g) = 4.07$  cgs,  $[\text{Fe}/\text{H}] = 0.02$  dex,  $V \sin i = 50$  km s<sup>-1</sup>) and contributes to the remaining 30%. Primary RVs derived in multiple-epoch fit are almost identical to ones estimated from fits for individual spectra. The derived mass ratio is  $q \sim 0.87$  and systemic radial velocity

$\gamma = -17.63$  km s<sup>-1</sup>. Additionally we make another multiple-epoch fit assuming same metallicity for both components, finding a slight change in  $T_{\text{eff}}$  and  $\log(g)$  with two components being metal-poor with  $[\text{Fe}/\text{H}] = -0.19$  dex. We can use  $q$  and  $\Delta \log(g)$  to estimate ratio of stellar sizes  $R_B/R_A = 0.73, 0.81$  for a solution with different and same metallicity. Additionally we fitted five out of 16 stacked spectra, previously analysed in Kovalev et al. (2022b). These spectra have significantly higher S/N (see bottom panel of Figure 2), but their lines are slightly blurred due to changes in RV. As a result we derived smaller metallicities ( $\Delta[\text{Fe}/\text{H}] \sim -0.07$  dex in comparison with short epochs results), although other parameters were almost identical to previous estimates for short epoch’s spectra. We present all spectroscopic results in the Table 4. The errors in the spectral parameters provided by `scipy.optimize.curve_fit` are nominal and largely underestimated. We also compared our spectral solutions for SB2 components with spectra, separated using other disentangling methods in Appendix E and found a good agreement.

In Figure 3 we show the best fits of the TESS 44 LCs (top) and RVs (bottom) by JKTEBOP. Fits for the ZTF  $r$  and TESS 45 can be found in Figures D1,D2. The fit residuals (O-C) are typically small ( $\leq 0.10$  mag for ZTF  $r$ ,  $\leq 0.02$  mag for TESS and  $\leq 5$  km s<sup>-1</sup> for RVs). Only one measurement for  $RV_B$  is off by  $\sim -15$  km s<sup>-1</sup>. The derived systemic velocities are very similar to the values derived from a multiple-epoch spectral fit. Orbital solutions for the primary star from GLS and JKTEBOP agree well, taking to account uncertainties. A very small value for the eccentricity ( $e \leq 0.002$ ) confirms that orbit is circular or very close to it. The orbital solution from Table 3 in Wang et al. (2021) has  $e = 1$  and  $K_A = 544$  km s<sup>-1</sup>, which is wrong due to failed optimisation. Third light contributions are significant in both TESS datasets (12 and 29 per cent) and negligible in ZTF  $r$ . This is not surprising due to the small aperture of TESS cameras relative to one in telescopes used for ZTF. The oblateness of the components (0.017, 0.007 for ZTF  $r$  and 0.013, 0.011 for TESS) is small ( $\leq 0.04$ ), thus JKTEBOP provides a reliable solution for this system (Popper & Etzel 1981). We show “corner” plots with all RP simulations in Figures D3,D4,D5, where correlations between fitted parameters can be explored. We present results from GLS and JKTEBOP in the Tables 2,3<sup>5</sup>

### 4.1 SED fitting

Spectral energy distribution (SED) can provide independent estimate of system’s parameters. We use published photometry and use out-of-eclipse measurements, when it is possible. To fit the SED we apply the `SPEEDYFIT` package<sup>6</sup>, which uses Kurucz (1979) models with a Markov chain Monte-Carlo approach to find the global minimum and determine the errors on the fit parameters. We set constraints on the solution using the Gaia DR3 parallax  $\varpi = 0.8915 \pm 0.0177$  mas, masses and radii from LC solution. Errors on the constraints are included as priors in the Bayesian fitting process and are thus propagated to the final results. A more detailed description of the fitting process is given in Vos et al. (2017). `SPEEDYFIT` doesn’t support ZTF and TESS filters, therefore we don’t use them. We show resulting fit in Figure 4 and list parameters in Table 5.  $T_{\text{eff}}$  values are slightly differ from spectroscopic ones, with residuals are within errors.

<sup>5</sup> Two additional LC datasets (ZTF  $g$  and ASAS-SN  $V$ ) were also fitted, but provided poor results inconsistent with ZTF  $r$ , TESS and spectroscopic fits ( $R_B > R_A$ ), possibly due to poor coverage of eclipses.

<sup>6</sup> <https://github.com/vosjo/speedyfit>

<sup>4</sup> JKTEBOP is written in FORTRAN77 and the source code is available at <http://www.astro.keele.ac.uk/jkt/codes/jktebop.html>



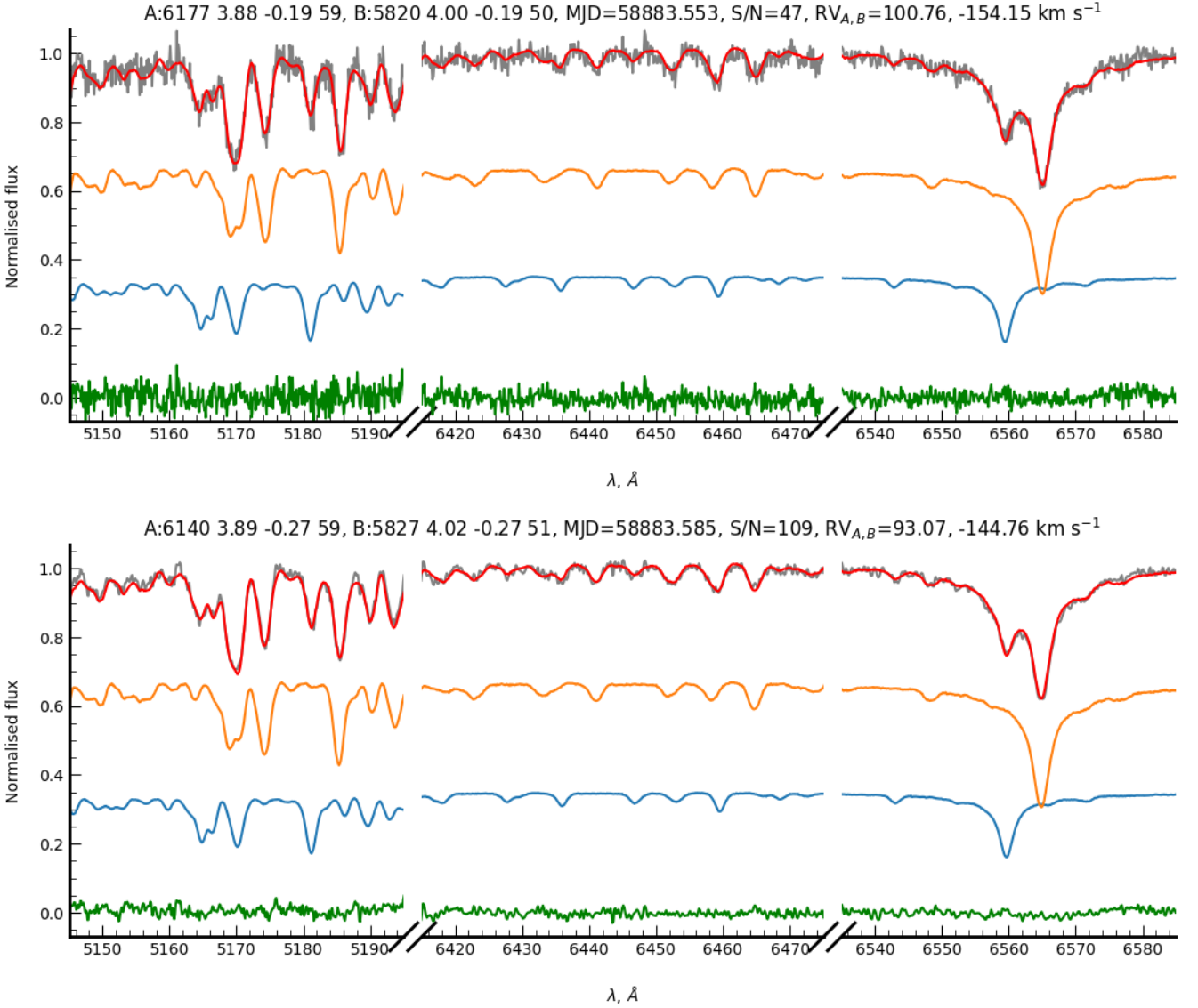


**Figure 2.** Example of the multiple-epoch fitting for short epochs spectra (top) and stacked spectra for whole night (bottom). The observed spectrum is shown as a gray line, the best fit is shown as red line. The primary component is shown as the orange line, the secondary as a blue line. The fit residuals are shown as a green line.

#### 4.2 Selection of SB2 candidates.

In Figure 5 we explore how the usage of the short epoch spectra can affect new SB2 selection method from Kovalev et al. (2022b). This method is based on  $V \sin i$  estimate from the single-star fit, and can detect SB2 with smaller  $|\Delta RV|$  than traditional methods, based on cross-correlation functions. We can see that all short epoch spectra below the blue line can be selected. All of them were observed in out of the eclipse phases. Derived sum of rotational velocities is nearly constant for them. Unlike stacked spectra we don't have any short epoch spectra, where single-star model fitted only one component. Two such stacked spectra are clearly seen in the bottom panel near upper left corner. Also we can clearly see, that linear relation derived in Kovalev et al. (2022b) for  $|\Delta RV|$  vs  $V \sin i_0$  is correct for short epoch spectra, observed in out of the eclipse phases, except for region with  $V \sin i_0 > 240 \text{ km s}^{-1}$ , where  $V \sin i_0$  "saturates".

## 5 DISCUSSION

### 5.1 System parameters

The physical parameters of the components suggests that the system consists two fast rotating stars, which are heavier and larger than the Sun. They form a close system with a circular orbit, slightly inclined to the line of sight, therefore we can see partial eclipses. Both components are on the main sequence and mass transfer is not started yet, as both components are smaller than their Roche lobes. The spectroscopic solution is computed with an assumption of the same  $[\text{Fe}/\text{H}]$  for both components have  $R_B/R_A = 0.81$  which is very close to the value  $R_B/R_A = 0.868 \pm 0.076$  from the TESS 44 LC fit. The relatively large projected rotational velocities measured from the spectra are in perfect agreement with  $V \sin i_{\text{sync } A,B} = 57.8 \pm 2.0, 50.0 \pm 2.5 \text{ km s}^{-1}$  computed using TESS LC fit parameters, suggesting spin-orbit synchronisation.

**Table 3.** JKTEBOP solutions for ZTF *r* and TESS LCs. Error's estimates are from RP simulations.

Parameter	ZTF <i>r</i>	TESS 44	TESS 45
fixed:			
Grav. darkening <sub>A</sub>	0.3108		0.2576
Grav. darkening <sub>B</sub>	0.3317		0.2760
Limb darkening $c_{A,i}$	0.3029, 0.8993, -0.7099, 0.2098	0.4002, 0.4901, -0.3288, 0.0638	
Limb darkening $c_{B,i}$	0.3420, 0.7173, -0.4286, 0.0838	0.4427, 0.3238, -0.0893, -0.0390	
fitted:			
<i>J</i>	0.762±0.025	0.770±0.005	0.772±0.019
$(R_A + R_B)/a$	0.3935±0.0065	0.4063±0.0013	0.4052±0.0033
$R_B/R_A$	0.667±0.065	0.868±0.076	0.840±0.152
$i^\circ$	83.77±1.74	81.66±0.29	81.13±0.74
$e \cos \omega$	0.0015±0.0009	0.0000±0.0001	0.0003±0.0003
$e \sin \omega$	-0.0018±0.0019	-0.0014±0.0019	-0.0021±0.0021
reflected light <sub>A</sub> , mag	0.010±0.005	-0.003±0.001	0.005±0.002
reflected light <sub>B</sub> , mag	0.010±0.005	0.003±0.001	0.010±0.002
$L_3$ , per cent	4.33 ± 9.87	12.04 ± 1.95	29.49 ± 3.93
$S_0$ , mag	13.586 ± 0.006	-0.009 ± 0.002	-5.546 ± 0.002
<i>P</i> , d	1.217783±0.000001	1.217785±0.000002	1.217785±0.000002
$t_0$ , HJD d	2458808.805418±0.000334	2458808.805166±0.000972	2458808.805001±0.000977
$K_A$ , km s <sup>-1</sup>	122.95±0.21	122.99±0.20	122.99±0.25
$K_B$ , km s <sup>-1</sup>	142.39±0.33	142.44±0.35	142.44±0.34
$\gamma_A$ , km s <sup>-1</sup>	-17.15±0.13	-17.04±0.11	-17.06±0.13
$\gamma_B$ , km s <sup>-1</sup>	-17.46±0.24	-17.59±0.22	-17.57±0.22
derived			
$L_B/L_A$	0.333±0.075	0.576±0.107	0.540±0.223
$e$	0.002±0.001	0.001±0.001	0.002±0.001
$\omega^\circ$	309.67±123.88	266.45±86.00	278.73±90.11
$a$ , $R_\odot$	6.425±0.022	6.457±0.010	6.466±0.016
$q$	0.863±0.003	0.863±0.003	0.863±0.003
$M_A$ , $M_\odot$	1.288±0.014	1.307±0.007	1.313±0.010
$M_B$ , $M_\odot$	1.112±0.011	1.129±0.005	1.133±0.008
$R_A$ , $R_\odot$	1.516±0.043	1.405±0.052	1.424±0.102
$R_B$ , $R_\odot$	1.012±0.077	1.219±0.060	1.196±0.123
log (g) <sub>A</sub> , cgs	4.186±0.025	4.259±0.033	4.249±0.065
log (g) <sub>B</sub> , cgs	4.474±0.057	4.319±0.042	4.337±0.086

Surface gravities derived by JKTEBOP are significantly larger than the spectroscopic ones. There is a bias of  $\Delta \log(g) = 0.3 - 0.4$  dex, which is larger than the expected  $\log(g)$  uncertainties given in Section 3.1.3. Similar bias was observed in Kovalev et al. (2019) for open cluster NGC 2243, where stars near the turn-off have spectroscopic  $\log(g)$  smaller than  $\log(g)$  from the PARSEC isochrone (Marigo et al. 2017). Thus such a bias can be related to the inaccuracy of the spectral models. Recent study by Chen et al. (2022) also noted underestimation of the  $\log(g)$  in LAMOST-MRS data when they are fitted by the binary model. Note that difference of spectroscopic surface gravities  $\log(g)_B - \log(g)_A = 0.12$  is comparable to difference  $(\log(g)_B - \log(g)_A = 0.06)$  from the TESS LC fit, because we use it to scale the relative contribution of the components in the spectrum.

We explore the previously reported measurements for this system and collect them in Table 6. Orbital periods from ZTF and ASAS-SN V are in good agreement with our estimations, although they are slightly shorter. The recent Gaia DR3 presents very interesting estimates by Multiple Star Classifier (MSC) Gaia Collaboration et al. (2022), where they tried to model observed low resolution *BP*, *RP* spectra using two stellar components. These estimates agree very well with our  $T_{\text{eff}}$  from the multiple-spectra fit and SED analysis and  $\log(g)$  from the TESS 44 dataset, although our  $[\text{Fe}/\text{H}]$  is 0.3-0.4 dex smaller. This is a well-behaved solution based on

goodness-of-fit score  $\text{logposterior\_msc}=495^7$ . We also retrieve all their 100 Monte Carlo samples and plot them in Figure F1.

Xiong et al. (2022) also used LAMOST-MRS, ZTF, ASAS-SN data to analyse this system with PHOEBE. For primary star in the system they got  $M_A$  and  $R_A$  larger than our estimates, but their  $T_{\text{eff}A}$  agrees with our value. For the secondary star their  $M_B$  is higher, but  $R_B$  and  $T_{\text{eff}B}$  are significantly smaller than our estimates. Their  $[\text{Fe}/\text{H}]$  for the system agrees with our estimate from the stacked spectra. We think that the disagreement is due to their usage of less precise LC datasets and the usage of spectral parameters from the second minimum observations for initialisation. They likely underestimated the orbital inclination, which led to much larger masses.

We take parameters from TESS 44 fit by JKTEBOP as a final solution as this LC has much better quality and greater quantity than other two. For  $T_{\text{eff}}$  and  $[\text{Fe}/\text{H}]$  we choose the result from multiple-epochs fit of short epochs with the same  $[\text{Fe}/\text{H}]$  for both components. Additionally we use PHOEBE to verify our results and find that ZTF

<sup>7</sup> [https://gea.esac.esa.int/archive/documentation/GDR3/Data\\_analysis/chap\\_cu8par/sec\\_cu8par\\_apsis/ssec\\_cu8par\\_apsis\\_msc.html](https://gea.esac.esa.int/archive/documentation/GDR3/Data_analysis/chap_cu8par/sec_cu8par_apsis/ssec_cu8par_apsis_msc.html)

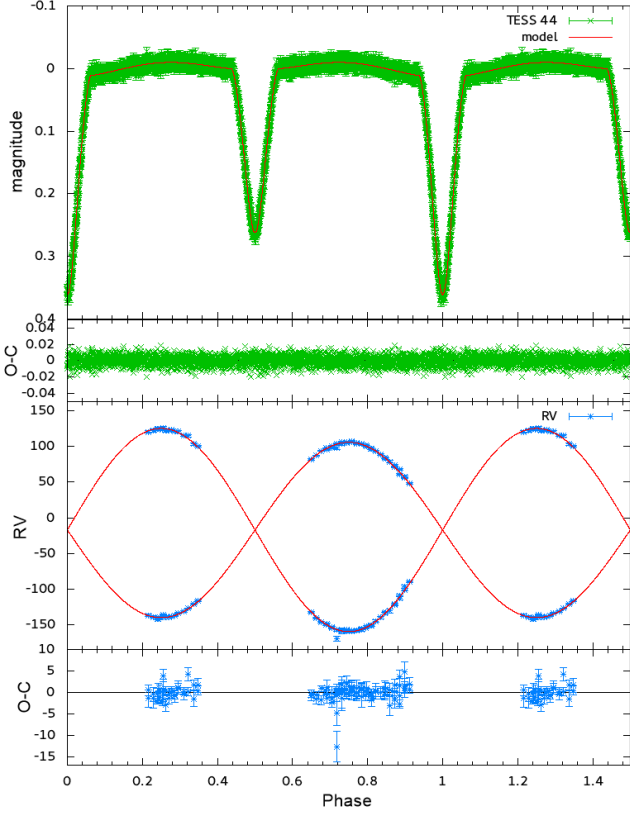


**Figure 3.** Phase-folded LC from TESS44 (top) and orbit (bottom) fits with JKTEBOP. In the bottom panels we show fit residuals O-C. The magnitudes are not calibrated.

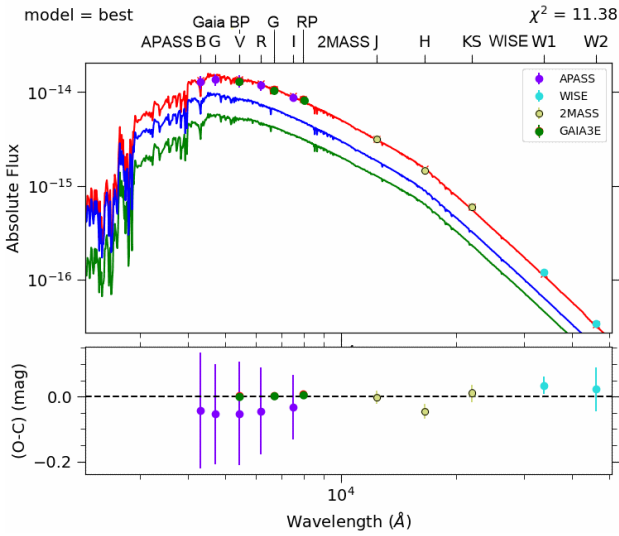


**Figure 4.** SED fitting with SPEEDYFIT. The top panels shows observations and spectral energy distribution of the system (red line), primary (blue line) and secondary (green line). The fit residuals are shown on the bottom panel.

**Table 4.** Spectral parameters from multiple-epoch fitting.

Parameter	Star A	Star B
short epoch's spectra with free [Fe/H]		
$\gamma$ , km s <sup>-1</sup>	-17.61 ± 0.28	
$q_{\text{dyn}}$	0.867 ± 0.005	
$T_{\text{eff}}$ , K	6104±13	5980±25
log (g), cgs	3.86±0.02	4.07±0.02
[Fe/H], dex	-0.29 ± 0.01	0.02±0.02
$V \sin i$ , km s <sup>-1</sup>	58±1	50±1
stacked spectra with free [Fe/H]		
$\gamma$ , km s <sup>-1</sup>	-17.34 ± 0.09	
$q_{\text{dyn}}$	0.866 ± 0.003	
$T_{\text{eff}}$ , K	6107±4	5941±9
log (g), cgs	3.86±0.01	4.07±0.01
[Fe/H], dex	-0.36 ± 0.01	-0.05±0.01
$V \sin i$ , km s <sup>-1</sup>	59±1	51±1
short epoch's spectra, assuming same [Fe/H]		
$\gamma$ , km s <sup>-1</sup>	-17.54 ± 0.28	
$q_{\text{dyn}}$	0.865 ± 0.005	
$T_{\text{eff}}$ , K	6177±9	5820±15
log (g), cgs	3.88±0.02	4.00±0.02
[Fe/H], dex	-0.19 ± 0.01	
$V \sin i$ , km s <sup>-1</sup>	59±1	50±1
stacked spectra, assuming same [Fe/H]		
$\gamma$ , km s <sup>-1</sup>	-17.32 ± 0.09	
$q_{\text{dyn}}$	0.866 ± 0.002	
$T_{\text{eff}}$ , K	6140±3	5827±6
log (g), cgs	3.89±0.01	4.02±0.01
[Fe/H], dex	-0.27 ± 0.01	
$V \sin i$ , km s <sup>-1</sup>	59±1	51±1

**Table 5.** SED fitting results and observed photometry from Gaia DR3 [Gaia Collaboration et al. \(2022\)](#), APASS [Henden et al. \(2015\)](#), 2MASS [Skrutskie et al. \(2006\)](#) and WISE [Cutri et al. \(2013\)](#). Gaia DR3 and WISE values were computed as mean and standard deviation of out-of-eclipse parts of the time-series.

Observations (mag):	
GDR3 <i>G</i>	13.416 ± 0.008
GDR3 <i>BP</i>	13.715 ± 0.009
GDR3 <i>RP</i>	12.949 ± 0.007
APASS <i>B</i>	14.22 ± 0.18
APASS <i>V</i>	13.61 ± 0.16
APASS <i>G</i>	13.90 ± 0.15
APASS <i>R</i>	13.45 ± 0.13
APASS <i>I</i>	13.32 ± 0.10
2MASS <i>J</i>	12.46 ± 0.02
2MASS <i>H</i>	12.22 ± 0.02
2MASS <i>K<sub>s</sub></i>	12.13 ± 0.03
WISE <i>W1</i>	12.08 ± 0.03
WISE <i>W2</i>	12.11 ± 0.07
Fitted parameters:	
$d$ , pc	1107 <sup>+12</sup> <sub>-11</sub>
$E(B - V)$ , mag	0.005 <sup>+0.039</sup> <sub>-0.029</sub>
$T_{\text{eff},A,B}$ , K	6006 <sup>+294</sup> <sub>-172</sub> , 5832 <sup>+316</sup> <sub>-199</sub>

*r* LC can be consistently fitted together with other two TESS LCs, see Appendix C.

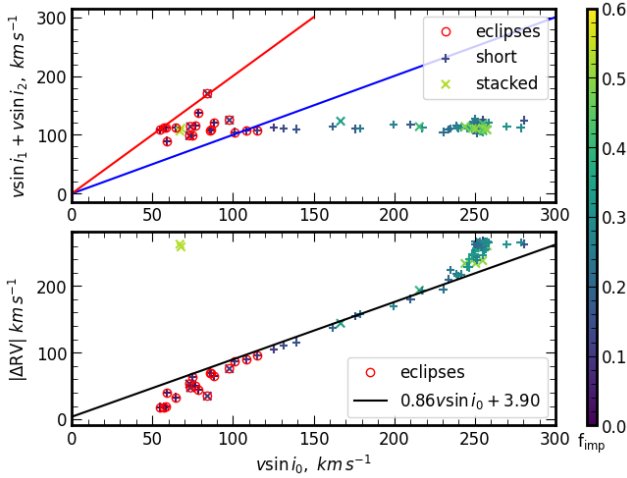


**Figure 5.**  $V \sin i_0$  values from the single-star fit versus  $V \sin i_1 + V \sin i_2$  from the binary fit (top panel) and versus  $|\Delta RV|$  (bottom panel). Blue and red solid lines show the functions  $V \sin i_1 + V \sin i_2 = V \sin i_0$  and  $V \sin i_1 + V \sin i_2 = 2V \sin i_0$  respectively. Black line shows best linear fit for a binary sample from Kovalev et al. (2022b). The data for spectra taken during eclipses are highlighted by the red open circles.

**Table 6.** Literature data compilation from ZTF Chen et al. (2020), ASAS-SN Jayasinghe et al. (2018), Gaia DR3 FLAME and Multiple Star Classifier (MSC) Gaia Collaboration et al. (2022), UNIDAM Mints & Hekker (2017) and Xiong et al. (2022). Gaia DR3 values provided with 16 and 84 percentiles. (\*) assuming single star.

Parameter	Value	reference
$P$ , d	1.2177044	ZTF
$P$ , d	1.217726	ASAS-SN
$d$ , pc	1080 <sup>1320</sup> <sub>10</sub>	GDR3 MSC
$A_G$ , mag	0.3131 <sup>0.9389</sup> <sub>0</sub>	GDR3 MSC
[Fe/H], dex	0.13 <sup>0.5</sup> <sub>-0.10</sub>	GDR3 MSC
$T_{\text{eff},A,B}$ , K	6127 <sup>7821</sup> <sub>5877</sub> , 5885 <sup>6558</sup> <sub>4018</sub>	GDR3 MSC
$\log(g)_{A,B}$ , cgs	4.28 <sup>5.52</sup> <sub>4.08</sub> , 4.57 <sup>5.2</sup> <sub>4.13</sub>	GDR3 MSC
$T_{\text{eff},A,B}$ , K	6193 ± 39, 5654 ± 57	Xiong
$\log(g)_{A,B}$ , cgs	4.09 ± 0.08, 4.64	Xiong
[Fe/H] <sub>A,B</sub> , dex	-0.250 ± 0.110	Xiong
$M_{A,B}$ , $M_{\odot}$	1.407 ± 0.011, 1.214 ± 0.011	Xiong
$R_{A,B}$ , $R_{\odot}$	1.501 ± 0.050, 0.868 ± 0.027	Xiong
$V \sin i_A$ , km s <sup>-1</sup>	91.80	Xiong
$q$	0.862 ± 0.015	Xiong
age t, Gyr	5.664 <sup>6.317</sup> <sub>4.983</sub>	GDR3 FLAME*
age log t, yr	9.572 ± 0.246	UNIDAM*

## 5.2 Age of the system

We use the grid of PARSEC isochrones (Marigo et al. 2017), computed at metallicity [Fe/H] = -0.19 dex, together with masses and radii from all RP simulations for the TESS 44 dataset to derive the system’s age, assuming that the two stars evolve separately, but have the same age. All fitted age solutions have median  $\log t = 9.195^{9.230}_{9.175}$  yr (1.56 Gyr) with 16 and 84 percentiles, which is significantly younger than the Sun. This is very different from the single star age values  $t = 5.664^{6.317}_{4.983}$  Gyr from GDR3 FLAME (Gaia Collaboration et al. 2022) and  $\log t = 9.572 \pm 0.246$  (3.73 Gyr) from (Mints & Hekker 2017). The theoretical circularisation time for an orbit with a given  $q$  and  $P$ , using Formula 6.2 from Zahn (1977):

$\log t_{\text{circ}} = 9.47$  yr (2.95 Gyr) is larger than our estimate of the system’s age, therefore tidal friction was very efficient and possibly was also accompanied by strong magnetic interactions. However we should note, that theoretical models have difficulty describing this system. In Figure 6 we plot a grid of PARSEC isochrones computed for [Fe/H] = -0.6, -0.2, 0.2 dex and five ages in a range from 1 to 5 Gyr. Our best fit isochrone is also shown, together with our best estimates and parameters from Xiong et al. (2022). Generally, theoretical models are steeper in the mass-radius plane than our estimates and therefore the best-fit isochrone goes through the upper errorbar for the primary and lower errorbar for the secondary. In the lower panel with the mass- $T_{\text{eff}}$  plane, you can see that theoretical values of  $T_{\text{eff}}$  are significantly larger than our  $T_{\text{eff}}$  estimates at corresponding masses. Only isochrones with significant super-solar metallicity will be able to match them. Therefore our results suggest that PARSEC isochrones are unable to model this close dEB system properly and our estimate of age is not reliable.

A similar discrepancy was found by Southworth (2022) for ZZ UMa, where PARSEC isochrones were not able to match all parameters in the system. For the secondary component the measured radius ( $R = 1.0752 \pm 0.0046 R_{\odot}$ ) is too large and the temperature ( $T_{\text{eff}} = 5270 \pm 90$  K) is too low in comparison with isochrone predictions, that well-match the primary component. Southworth (2022) suggest that this is case of *radius discrepancy*, which is well-known phenomena for the late-type dwarfs.

Recently del Burgo & Allende Prieto (2018) employed a set of well studied dEBs to test PARSEC isochrones, using a Bayesian framework to infer masses, distances and ages, taking radii,  $T_{\text{eff}}$  and [Fe/H] as input. They found that PARSEC models systematically underestimate masses, although discrepancies are not so important for the main sequence. For example, the close dEB system UZ Dra with similar parameters to J064726.39+223431.6 ( $P = 3.261$  d,  $R_{A,B} = 1.31 \pm 0.03, 1.15 \pm 0.02 R_{\odot}$ ,  $T_{\text{eff},A,B} = 6209 \pm 114, 5984 \pm 110$  K,  $M_{A,B} = 1.34 \pm 0.02, 1.23 \pm 0.02 M_{\odot}$ , no estimate of [Fe/H] yet) they inferred  $M_{A,B}^{\text{fit}} = 1.13 \pm 0.09, 1.04 \pm 0.09 M_{\odot}$ , assuming solar metallicity for this system.

Additionally we check another two sets of theoretical models by Dotter (2016) and Claret (2019), but find no improvement relative to PARSEC.

## 6 CONCLUSIONS

We present a study of the dEB SB2 J064726.39+223431.6 system using spectra from the LAMOST-MRS survey and photometrical data. We use full-spectrum fitting to derive radial velocities and spectral parameters. The orbital solution and light curves from ZTF and TESS suggest that it is a close pair on a circular orbit. We have measured the masses of the stars to accuracies of 1 per cent and the radii to accuracies of 5 per cent. The system shows strong evidence for spin-orbit synchronisation. We find a discrepancy between spectroscopic  $\log(g)$  and  $\log(g)$  calculated using parameters from the LC fitting. We found that [Fe/H] derived from the stacked spectra is 0.07 dex smaller than [Fe/H] calculated using short epochs. Theoretical isochrones also unable to model the measured mass- $T_{\text{eff}}$  relations at derived metallicity. The derived age of the system indicates that both components are still on the main sequence, although it is much shorter than orbit’s circularisation timescale.



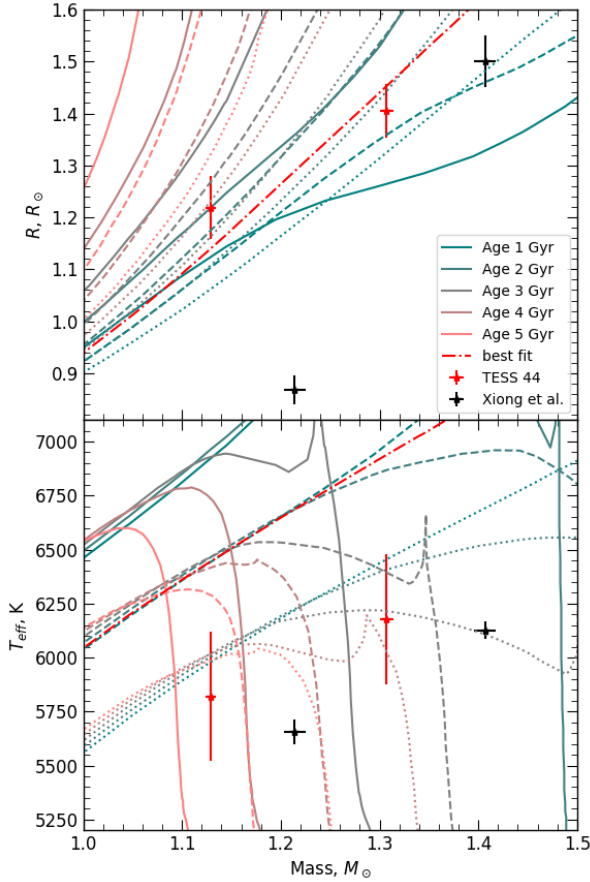


**Figure 6.** The grid of PARSEC isochrones computed for  $[Fe/H] = -0.6$  (solid lines),  $-0.2$  (dashed lines),  $0.2$  dex (dotted lines) and five ages in range from 1 to 5 Gyr. Our best fit ( $[Fe/H] = -0.19$  dex, age 1.57 Gyr) isochrone is also shown (red dot-dashed line), together with our best estimates and parameters from Xiong et al. (2022).

**ACKNOWLEDGEMENTS**

We are grateful to the anonymous referee for a constructive report. We thank Hans Bähr for his careful proof-reading of the manuscript. We thank Saša Ilijić for help with FD3 code. MK is grateful to his parents, Yuri Kovalev and Yulia Kovaleva, for their full support in making this research possible. The work is supported by the Natural Science Foundation of China (Nos. 11733008, 12090040, 12090043, 11521303, 12125303, 12273057). S. W. acknowledges support from the Youth Innovation Promotion Association of the CAS (id. 2019057). Guoshoujing Telescope (the Large Sky Area Multi-Object Fiber Spectroscopic Telescope LAMOST) is a National Major Scientific Project built by the Chinese Academy of Sciences. Funding for the project has been provided by the National Development and Reform Commission. LAMOST is operated and managed by the National Astronomical Observatories, Chinese Academy of Sciences. The authors gratefully acknowledge the “PHOENIX Supercomputing Platform” jointly operated by the Binary Population Synthesis Group and the Stellar Astrophysics Group at Yunnan Observatories, Chinese Academy of Sciences. This research has made use of NASA’s Astrophysics Data System, the SIMBAD data base, and the VizieR catalogue access tool, operated at CDS, Strasbourg, France. It also made use of TOPCAT, an interactive graphical viewer and editor for tabular data (Taylor 2005). Funding for the TESS mission is provided by

NASA’s Science Mission directorate. This paper includes data collected by the TESS mission, which is publicly available from the Mikulski Archive for Space Telescopes (MAST). This work has made use of data from the European Space Agency (ESA) mission *Gaia* (<https://www.cosmos.esa.int/gaia>), processed by the *Gaia* Data Processing and Analysis Consortium (DPAC, <https://www.cosmos.esa.int/web/gaia/dpac/consortium>). Funding for the DPAC has been provided by national institutions, in particular the institutions participating in the *Gaia* Multilateral Agreement.

Based on observations obtained with the Samuel Oschin Telescope 48-inch and the 60-inch Telescope at the Palomar Observatory as part of the Zwicky Transient Facility project. ZTF is supported by the National Science Foundation under Grant No. AST-2034437 and a collaboration including Caltech, IPAC, the Weizmann Institute for Science, the Oskar Klein Center at Stockholm University, the University of Maryland, Deutsches Elektronen-Synchrotron and Humboldt University, the TANGO Consortium of Taiwan, the University of Wisconsin at Milwaukee, Trinity College Dublin, Lawrence Livermore National Laboratories, and IN2P3, France. Operations are conducted by COO, IPAC, and UW This research has made use of the NASA/IPAC Infrared Science Archive, which is funded by the National Aeronautics and Space Administration and operated by the California Institute of Technology.

**DATA AVAILABILITY**

The data underlying this article will be shared on reasonable request to the corresponding author.

**REFERENCES**

Andersen J., 1991, *A&ARv*, 3, 91  
 Brasseur C. E., Phillip C., Fleming S. W., Mullally S. E., White R. L., 2019, *Astrocut: Tools for creating cutouts of TESS images*, Astrophysics Source Code Library, record ascl:1905.007 (ascl:1905.007)  
 Chen X., Wang S., Deng L., de Grijs R., Yang M., Tian H., 2020, *ApJS*, 249, 18  
 Chen X.-L., Luo A.-L., Chen J.-J., Wang R., Zhang X.-B., Hou W., Qiu B., Zuo F., 2022, arXiv e-prints, p. [arXiv:2209.10714](https://arxiv.org/abs/2209.10714)  
 Claret A., 2017, *A&A*, 600, A30  
 Claret A., 2019, *A&A*, 628, A29  
 Claret A., Bloemen S., 2011, *A&A*, 529, A75  
 Conroy K. E., et al., 2020, *ApJS*, 250, 34  
 Cui X.-Q., et al., 2012, *Research in Astronomy and Astrophysics*, 12, 1197  
 Cutri R. M., et al., 2013, Explanatory Supplement to the AllWISE Data Release Products, Explanatory Supplement to the AllWISE Data Release Products, by R. M. Cutri et al.  
 Czesla S., Schröter S., Schneider C. P., Huber K. F., Pfeifer F., Andreasen D. T., Zechmeister M., 2019, *PyA: Python astronomy-related packages* (ascl:1906.010)  
 Dotter A., 2016, *ApJS*, 222, 8  
 Eker Z., et al., 2015, *AJ*, 149, 131  
 Eker Z., et al., 2018, *MNRAS*, 479, 5491  
 El-Badry K., et al., 2018, *MNRAS*, 476, 528  
 Feinstein A. D., et al., 2019, *PASP*, 131, 094502  
 Foreman-Mackey D., 2016, *The Journal of Open Source Software*, 1, 24  
 Gaia Collaboration et al., 2022, arXiv e-prints, p. [arXiv:2208.00211](https://arxiv.org/abs/2208.00211)  
 González J. F., Levato H., 2006, *A&A*, 448, 283  
 Grupp F., 2004a, *A&A*, 420, 289  
 Grupp F., 2004b, *A&A*, 426, 309  
 Han Z.-W., Ge H.-W., Chen X.-F., Chen H.-L., 2020, *Research in Astronomy and Astrophysics*, 20, 161

- Henden A. A., Levine S., Terrell D., Welch D. L., 2015, in *American Astronomical Society Meeting Abstracts #225*. p. 336.16
- Ilijic S., 2017, fd3: Spectral disentangling of double-lined spectroscopic binary stars, *Astrophysics Source Code Library*, record ascl:1705.012 (ascl:1705.012)
- Ilijic S., Hensberge H., Pavlovski K., Freyhammer L. M., 2004, in Hilditch R. W., Hensberge H., Pavlovski K., eds, *Astronomical Society of the Pacific Conference Series Vol. 318, Spectroscopically and Spatially Resolving the Components of the Close Binary Stars*. pp 111–113
- Jayasinghe T., et al., 2018, *MNRAS*, **477**, 3145
- Kovalev M., 2019, PhD thesis, Heidelberg University, doi:10.11588/heidok.00027411
- Kovalev M., Bergemann M., Ting Y.-S., Rix H.-W., 2019, *A&A*, **628**, A54
- Kovalev M., Li Z., Zhang X., Li J., Chen X., Han Z., 2022a, *MNRAS*, **513**, 4295
- Kovalev M., Chen X., Han Z., 2022b, *MNRAS*, **517**, 356
- Kurucz R. L., 1979, *ApJS*, **40**, 1
- Liu C., et al., 2020, arXiv e-prints, p. arXiv:2005.07210
- Marigo P., et al., 2017, *ApJ*, **835**, 77
- McLaughlin D. B., 1924, *ApJ*, **60**, 22
- Mints A., Hekker S., 2017, *A&A*, **604**, A108
- Pavlovski K., et al., 2022, *A&A*, **658**, A92
- Popper D. M., Etzel P. B., 1981, *AJ*, **86**, 102
- Qian S.-B., et al., 2019, *Research in Astronomy and Astrophysics*, **19**, 064
- Quintero E. A., Eenens P., Rauw G., 2020, *Astronomische Nachrichten*, **341**, 628
- Ricker G. R., et al., 2015, *Journal of Astronomical Telescopes, Instruments, and Systems*, **1**, 014003
- Rossiter R. A., 1924, *ApJ*, **60**, 15
- Skrutskie M. F., et al., 2006, *AJ*, **131**, 1163
- Southworth J., 2013, *A&A*, **557**, A119
- Southworth J., 2015, in Rucinski S. M., Torres G., Zejda M., eds, *Astronomical Society of the Pacific Conference Series Vol. 496, Living Together: Planets, Host Stars and Binaries*. p. 164 (arXiv:1411.1219)
- Southworth J., 2022, arXiv e-prints, p. arXiv:2209.10384
- Southworth J., Pavlovski K., Tamajo E., Smalley B., West R. G., Anderson D. R., 2011, *MNRAS*, **414**, 3740
- Stassun K. G., et al., 2019, *AJ*, **158**, 138
- Taylor M. B., 2005, in Shopbell P., Britton M., Ebert R., eds, *Astronomical Society of the Pacific Conference Series Vol. 347, Astronomical Data Analysis Software and Systems XIV*. p. 29
- Ting Y.-S., Conroy C., Rix H.-W., Cargile P., 2019, *ApJ*, **879**, 69
- Torres G., 2021, *Research Notes of the American Astronomical Society*, **5**, 256
- Torres G., Andersen J., Giménez A., 2010, *A&ARv*, **18**, 67
- Vos J., Østensen R. H., Vučković M., Van Winckel H., 2017, *A&A*, **605**, A109
- Wang S., et al., 2021, *Research in Astronomy and Astrophysics*, **21**, 292
- Watson C. L., Henden A. A., Price A., 2006, *Society for Astronomical Sciences Annual Symposium*, **25**, 47
- Xiong J., et al., 2022, arXiv e-prints, p. arXiv:2211.08647
- Zahn J. P., 1977, *A&A*, **57**, 383
- Zechmeister M., Kürster M., 2009, *A&A*, **496**, 577
- Zhao G., Zhao Y.-H., Chu Y.-Q., Jing Y.-P., Deng L.-C., 2012, *Research in Astronomy and Astrophysics*, **12**, 723
- del Burgo C., Allende Prieto C., 2018, *MNRAS*, **479**, 1953

## APPENDIX A: SPECTRAL MODELS

The synthetic spectra are generated using NLTE MPIA online-interface <https://nlte.mpia.de> (see Chapter 4 in Kovalev 2019) on wavelength intervals 4870:5430 Å for the blue arm and 6200:6900 Å for the red arm with spectral resolution  $R = 7500$ . We use NLTE (non-local thermodynamic equilibrium) spectral synthesis for H, Mg I, Si I, Ca I, Ti I, Fe I and Fe II lines (see Chapter 4 in Kovalev 2019, for references).

The grid of models (6200 in total) is computed for points randomly selected in a range of  $T_{\text{eff}}$  between 4600 and 8800 K,  $\log(g)$  between 1.0 and 4.8 (cgs units),  $V \sin i$  from 1 to 300 km s<sup>-1</sup> and [Fe/H]<sup>8</sup> between -0.9 and +0.9 dex. The model is computed only if linear interpolation of the MAFAGS-OS(Grupp 2004a,b) stellar atmosphere is possible for a given point in parameter space. Microturbulence is fixed to  $V_{\text{mic}} = 2$  km s<sup>-1</sup> for all models. The grid is randomly split on training (70%) and cross-validation (30%) sets of spectra, which are used to train *The Payne* spectral model (Ting et al. 2019). The neural network (NN) consists of two layers of 300 neurons each with rectilinear unit (ReLU)<sup>9</sup> activation functions. We train separate NNs for each spectral arm. The median approximation error is less than 1% for both arms. We use output of *The Payne* as single-star spectral model.

## APPENDIX B: RV MEASUREMENTS

We provide RV measurements from the short epochs in Table B1.

## APPENDIX C: VERIFICATION WITH PHOEBE

We use PHOEBE(Conroy et al. 2020) to verify our results, since it allows one to fit multiple LC datasets simultaneously, and updates limb darkening coefficients during the fitting. For all three LCs we convert magnitudes to fluxes and divide them by the median value. We also subtract the best fit  $t_0$  from the timescale in all datasets. We use the default Nelder-Mead optimiser and default “ck2004” atmospheres. Eccentricity, period and mass ratio were fixed, thus we fit for  $R_{A,B}$ ,  $T_{\text{eff}A,B}$ ,  $\gamma$ ,  $a \sin i$ ,  $i$  and the third light contribution for three LC datasets.

We present fitting results in Figure C1 and Table C1. The best fit PHOEBE model fits all three LCs well since the residuals (O-C) are insignificant. All parameters agree with JKTEBOP values for TESS datasets, therefore our usage of fixed limb darkening coefficients is reasonable. The best fit  $T_{\text{eff}B}$  of the secondary agrees with the spectroscopic estimate, but  $T_{\text{eff}A}$  is 250 K higher. The computed  $V \sin i$  are in excellent agreement with spectroscopic values. We don’t use any sampling techniques to estimate errors as PHOEBE calculations are very computationally expensive in comparison with JKTEBOP, but we think uncertainties will be slightly smaller than ones, provided by PHOEBE in Xiong et al. (2022).

By phase-folding the whole RV dataset we find that several spectra were taken exactly during eclipses. In Figure C2 we show RVs measured from these spectra together with the flux-weighted RV curves computed by PHOEBE using the best parameters. We can see that RM effect is not very strong, but it can be barely seen in our RVs data for primary eclipse, therefore eclipse is not total.

## APPENDIX D: RESIDUAL-PERMUTATION SIMULATIONS

Fits for the ZTF  $r$  and TESS 45 LC datasets can be found in Figures D1,D2.

In Figures D3, D4, D5 we show corner plots (Foreman-Mackey 2016) with all residual-permutation simulation results for

<sup>8</sup> We used [Fe/H] as a proxy of overall metallicity, abundances for all elements are scaled with Fe.

<sup>9</sup>  $\text{ReLU}(x)=\max(x,0)$

**Table B1.** Radial velocity measurements. The asterisk (\*) denotes data-points which are not used in analysis with GLS and JKTEBOP. We subtract 2400000.5 days from time values.

time HJD d	ind. epoch $RV_B, RV_A$ $\text{km s}^{-1}$	single RV $\text{km s}^{-1}$
58806.744	98.54±2.07, -169.77±2.50	-7.01
58806.760	103.66±1.71, -159.21±2.72	-1.42
58806.776	-159.98±1.02, 106.50±0.70	-5.79
58806.792	-158.66±1.12, 106.87±0.80	2.57
58806.808	-158.83±0.97, 103.80±0.68	-5.38
58806.825	-155.77±1.06, 103.79±0.72	-7.45
58806.841	-152.48±1.11, 100.31±0.72	-0.87
58806.857	-151.16±1.10, 96.59±0.79	-9.72
58820.774	124.71±0.89, -141.97±0.66	-20.69
58820.783	124.27±0.97, -139.47±0.66	-26.77
58820.792	123.54±0.92, -140.18±0.64	-21.63
58820.802	121.96±1.00, -139.56±0.69	-23.36
58820.811	122.94±1.00, -139.70±0.73	-16.79
58820.820	123.32±0.92, -138.43±0.68	-19.63
58820.830	121.06±1.01, -137.90±0.67	-26.18
58835.736	-40.86±2.70, 3.96±1.90*	-12.50
58835.753	-45.46±1.58, 24.66±1.34*	-9.52
58835.769	-64.15±1.63, 22.22±1.08*	-9.63
58835.785	30.49±0.91, -74.37±1.36*	-10.97
58856.640	-149.11±1.20, 96.22±0.84	0.62
58856.656	-154.25±1.13, 98.60±0.87	-8.63
58856.672	-157.34±1.25, 104.05±0.90	-2.07
58856.688	-157.91±0.99, 105.83±0.71	-12.86
58856.704	-158.98±1.20, 105.49±0.84	-6.12
58856.720	-158.31±1.05, 106.23±0.83	-12.57
58860.669	-9.49±2.36, -27.99±3.65*	-16.65
58860.685	0.21±2.98, -39.85±3.50*	-21.37
58860.701	9.52±3.42, -41.39±2.49*	-20.35
58860.717	25.16±2.84, -43.71±1.84*	-22.23
58883.558	-154.79±0.85, 101.26±0.63	-8.13
58883.574	-151.01±0.91, 96.86±0.67	-8.01
58883.590	-145.40±1.23, 93.86±0.88	-8.07
58883.606	-140.24±1.00, 88.86±0.72	-8.89
58883.623	83.10±0.72, -132.46±0.95	-13.08
58889.536	-155.40±0.78, 100.59±0.59	-6.28
58889.552	-157.68±0.91, 103.44±0.63	-9.97
58889.568	-158.45±1.17, 106.64±0.86	-3.32
58889.585	-157.72±1.20, 105.39±0.87	-5.89
58889.601	-159.82±1.15, 106.04±0.86	-10.49
58889.617	-157.74±1.38, 104.89±1.03	-7.40
58889.634	-157.47±1.70, 103.59±1.28	-7.53
58919.483	120.69±1.05, -134.31±0.73	-25.05
58919.500	115.05±0.93, -131.58±0.65	-23.05
58919.516	115.08±1.11, -127.50±0.75	-13.90
58919.533	103.32±1.31, -120.86±0.84	-25.18
58919.548	100.36±1.10, -116.91±0.76	-17.02

$J, R_B/R_A, i, L_B/L_A,$  and  $\log(g)_{A,B}$  for ZTF  $r$  and TESS LCs. There is strong correlation between  $J$  and  $R_B/R_A$  clearly visible for all datasets, which can propagate into other parameters like  $L$  and  $\log(g)$ . However the most precise TESS 44 dataset is less affected.

**APPENDIX E: SPECTRAL SEPARATION.**

There are many spectral separation/disentangling methods available in the literature, so we tested two of them: “shift and add” and Fourier separation on the spectra of our SB2 system.

**Table B1 – continued**

HJD d	ind. epoch $RV_B, RV_A$ $\text{km s}^{-1}$	single RV $\text{km s}^{-1}$
59149.811	42.48±1.03, -67.68±0.75*	-26.09
59149.827	29.63±1.34, -61.11±0.89*	-27.31
59149.843	-63.52±1.05, 1.57±1.21*	-25.46
59149.859	24.68±2.57, -39.14±1.14*	-24.76
59149.876	-3.04±2.01, -36.29±1.66*	-21.09
59149.892	-28.63±2.69, -10.16±1.36*	-15.98
59149.905	-25.12±3.82, -5.62±2.65*	-13.35
59180.759	-134.31±1.42, 84.06±1.00	-7.81
59180.775	78.87±1.14, -130.97±1.68	-15.45
59180.791	-121.85±1.40, 73.23±1.03	-14.22
59180.807	-112.51±1.68, 67.83±1.22	-4.65
59180.824	-97.08±1.62, 57.49±1.27	-14.16
59189.734	120.61±1.38, -136.89±0.94	-22.00
59189.750	122.79±1.66, -139.65±1.24	-16.01
59189.767	125.09±1.54, -141.53±1.06	-13.64
59189.783	125.75±1.80, -136.33±1.12	-12.49
59235.592	-121.19±0.94, 71.44±0.65	-9.07
59235.609	-109.18±1.12, 60.83±0.72	-12.97
59235.625	56.43±0.75, -101.27±1.09	-13.91
59235.641	47.93±0.71, -89.90±1.06	-14.00
59235.664	-79.47±1.01, 36.19±0.75*	-14.24
59235.680	27.45±0.92, -68.23±1.29*	-9.16
59264.548	-133.20±0.93, 82.00±0.67	-10.98
59264.564	-140.56±0.82, 87.29±0.57	-15.60
59264.580	-146.59±0.76, 93.68±0.54	-10.64
59264.597	-150.17±0.78, 97.62±0.59	-8.63

**Table C1.** Parameters derived by PHOEBE when fitting all three LCs simultaneously

Parameter	Star A	Star B
fixed		
$q$		0.87
$P, \text{d}$		1.21778
$e$		0.00
fitted		
$\gamma, \text{km s}^{-1}$		-17.25
$i^\circ$		81.63
$a \sin i, R_\odot$		6.421
$R_{\text{equiv}}, R_\odot$	1.427	1.219
$T_{\text{eff}}, \text{K}$	6414	5873
$L_3 \text{ ZTF } r, \text{ per cent}$		0.0
$L_3 \text{ TESS } 44, \text{ per cent}$		12.0
$L_3 \text{ TESS } 45, \text{ per cent}$		30.4
derived		
$M, M_\odot$	1.323	1.151
$\log(g), \text{cgs}$	4.251	4.327
$V \sin i, \text{km s}^{-1}$	58.67	50.10

We used the “shift and add” algorithm described in [González & Levato \(2006\)](#) to extract rest-frame spectra for both components. We selected 24 spectra with  $S/N \geq 40$  and  $\Delta RV > 180 \text{ km s}^{-1}$ . All these spectra were previously normalised during the binary model fitting as described in Section 3.1.1. Radial velocities were computed using the orbital solution. Spectral components were found via iterative subtraction of the weighted sum of the Doppler-shifted spectra from the original flat baseline spectra, which were set to

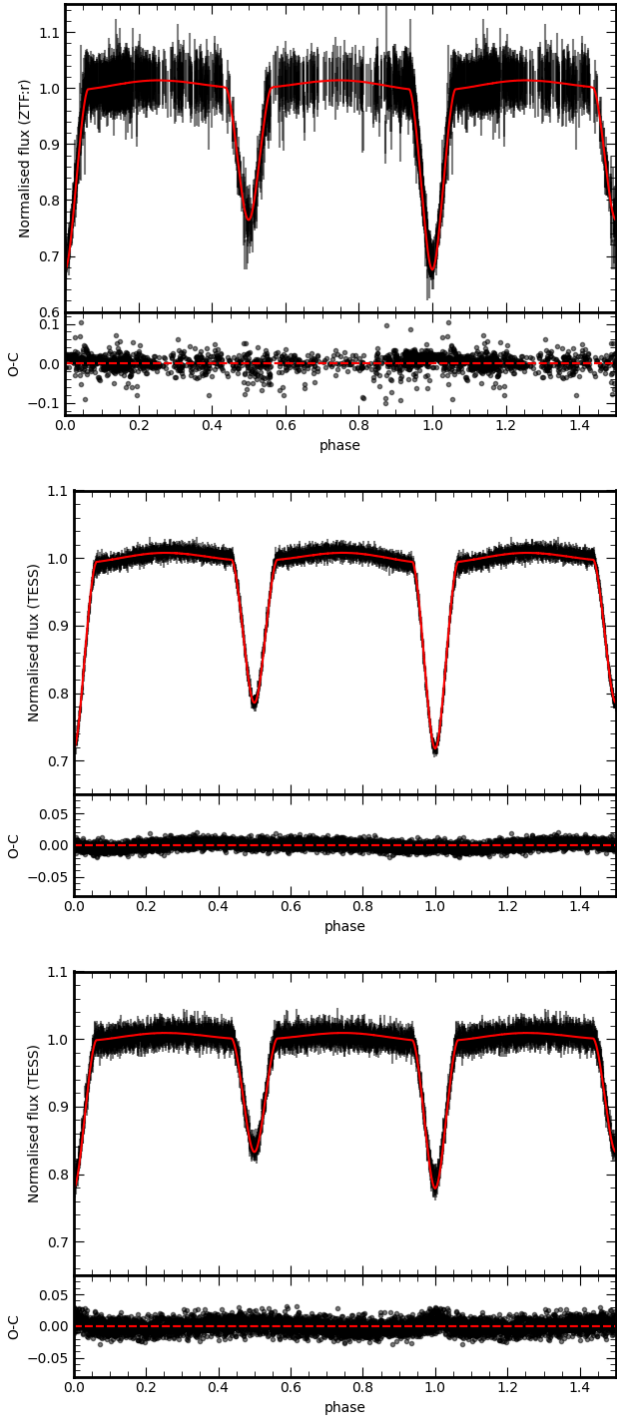


**Figure C1.** The best fit PHOEBE model for ZTF *r* (top), TESS 44 (middle) and TESS 45 (bottom) LCs.

0.5. The seven iterations were enough to clearly reveal both spectral components, except for the spectral edges, where solutions start to oscillate around the baseline. This approach can utilize errors of the original spectra and efficiently remove spectral artifacts, like contamination by cosmic rays.

For the Fourier separation we used FD3 code (Ilijić 2017). This code can do disentangling of up to three spectral components

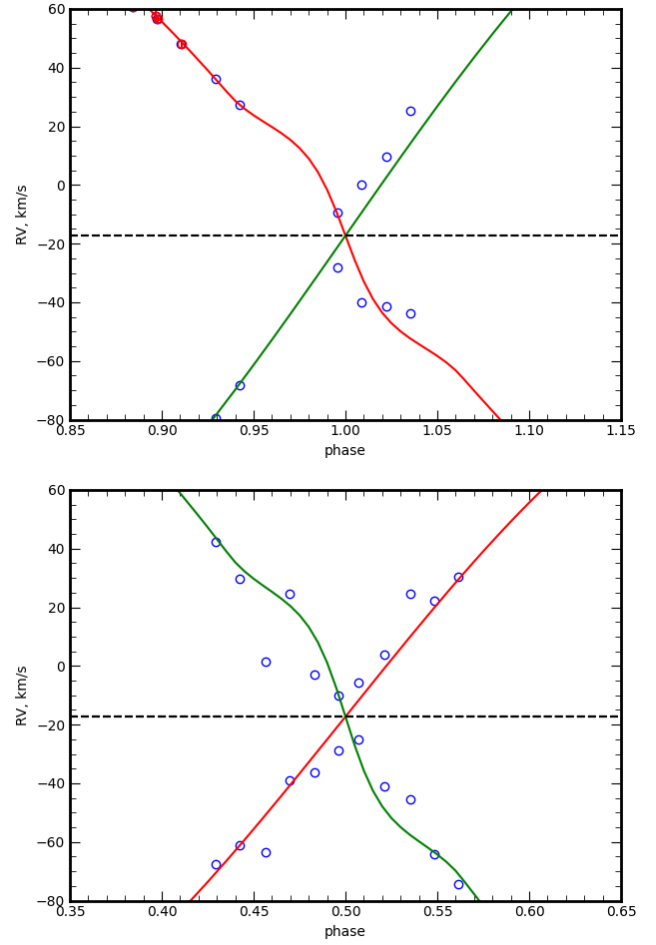


**Figure C2.** Radial velocities measured during eclipses together with best fit PHOEBE model for primary (red line) and secondary (green line) components. Blue datapoints were not used in the fit.

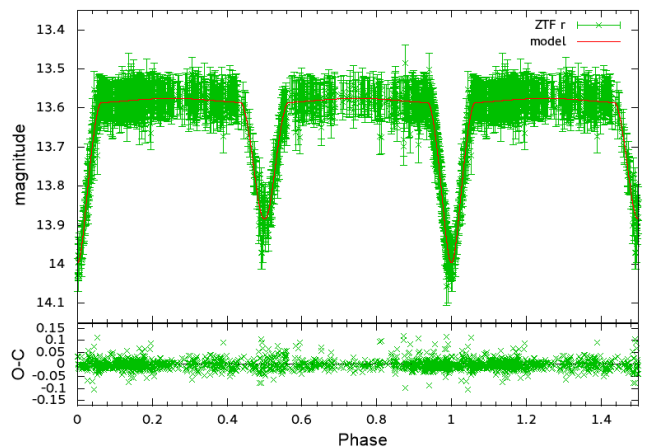


**Figure D1.** Phase-folded LC from ZTF *r* fit with JKTEBOP. In the bottom panels we show fit residuals.



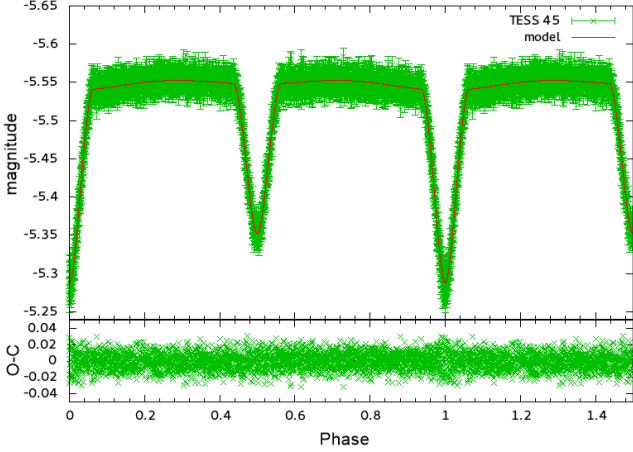


**Figure D2.** Phase-folded LC from TESS45 fit with JKTEBOP. In the bottom panels we show fit residuals. The magnitudes are not calibrated.

**Table E1.** FD3 orbital solution for stacked spectra. Unfortunately FD3 don't provide any uncertainties.

Parameter	Blue	Red
$P$ , d	1.217784	1.217784
$t_0$ , HJD d	2458808.034	2458808.034
$K_A$ , km s <sup>-1</sup>	121.83	120.92
$K_B$ , km s <sup>-1</sup>	141.62	140.18
$e$	0.02	0.02
$\omega^\circ$	39.95	41.7

simultaneously with the orbital fitting for inner binary system. We found out that spectral artifacts, like cosmic rays spikes, will contaminate resulting spectra, thus we used code with stacked spectra, which have been already cleaned. Blue and red parts of the spectra were analysed separately. We used 14 spectra taken in the out-of-eclipse phases with the light factors  $LF = 1$  for both components, thus resulting spectra should have the baseline 0.5. Derived orbital parameters are listed in Table E1. They are consistent with the GLS and JKTEBOP orbital solutions, although  $K$  and  $e$  were slightly different, possibly due to usage of the stacked spectra. The resulting separated spectra showed the smooth undulations, which were removed following the steps in Ilijic et al. (2004).

We show the best-fit multiple-epoch spectral models with the separation results from both methods in Figure E1. Note, that the Fourier separation spectra are blue-shifted according to  $\gamma$ , since this parameter was not included in orbital solution. Generally agreement is good for FD3 results, while “shift and add” separation show large difference around  $H\alpha$ . Such bad performance on the broad lines is known for this method (Quintero et al. 2020).

We tried to fit the FD3 separated spectra by the single-star spectral model, but found the poor results for the secondary, not consistent with the LC, SED and multiple-spectra solutions. We used root mean square error of disentangling residuals as an error for the separated spectra, equal for both components. When we fitted for spectral parameters and light factors  $LF_i$  (one for each blue and red spectral parts) we found good fits with significant difference in the metallicity  $\Delta[\text{Fe}/\text{H}] > 0.5$  dex between components. Also the derived light factors were not consistent for the primary and the sec-

ondary ( $LF_A + LF_B \neq 1$ ) for both blue and red parts of the spectra. We repeated fitting, fixing the light factors to values  $LF_A, LF_B = 0.65, 0.35$  and keep  $\log(g)_{A,B} = 4.26, 4.32$  (cgs) equal to values from the TESS 44 LC solution. We got a solution with  $T_{\text{eff},A,B} = 6070 \pm 36, 6046 \pm 64$  K,  $[\text{Fe}/\text{H}]_{A,B} = -0.37 \pm 0.03, -0.15 \pm 0.05$  dex and  $V \sin i_{A,B} = 63 \pm 3, 54 \pm 3$  km s<sup>-1</sup>, see Figure E2. This result is similar to the SED temperatures and spectral parameters derived from the stacked spectra using the multiple-epoch fitting. The spectral separation methods require more prior information ( $LF$  or orbital solution) in comparison with multiple-epochs fitting, therefore we prefer later one for analysis on LAMOST-MRS data. However for very high-quality spectra of the bright stars spectral separation can give reasonable  $LF$  (see Pavlovski et al. 2022, analysis of  $\alpha$  Dra).

**APPENDIX F: GAIA DR3 MONTE CARLO MULTIPLE STAR CLASSIFIER SAMPLE**

In Figure F1 we show corner plot (Foreman-Mackey 2016) with Monte Carlo Multiple Star Classifier sample from Gaia Collaboration et al. (2022). We select a subsample with  $A_0 > 0.2$  mag (70 datapoints). These results have higher  $\log_{\text{post}}$ . We compute 16, 50 and 84 percentiles for them and the median values are comparable to our final parameters, however metallicity and  $\log(g)_B$  are higher. The remaining 30 datapoints with smaller  $\log_{\text{post}}$  have  $\log(g)_{A,B} \sim 4.7$  cgs. This is probably solutions from local maximum of the posterior.

This paper has been typeset from a  $\text{\TeX}/\text{\LaTeX}$  file prepared by the author.

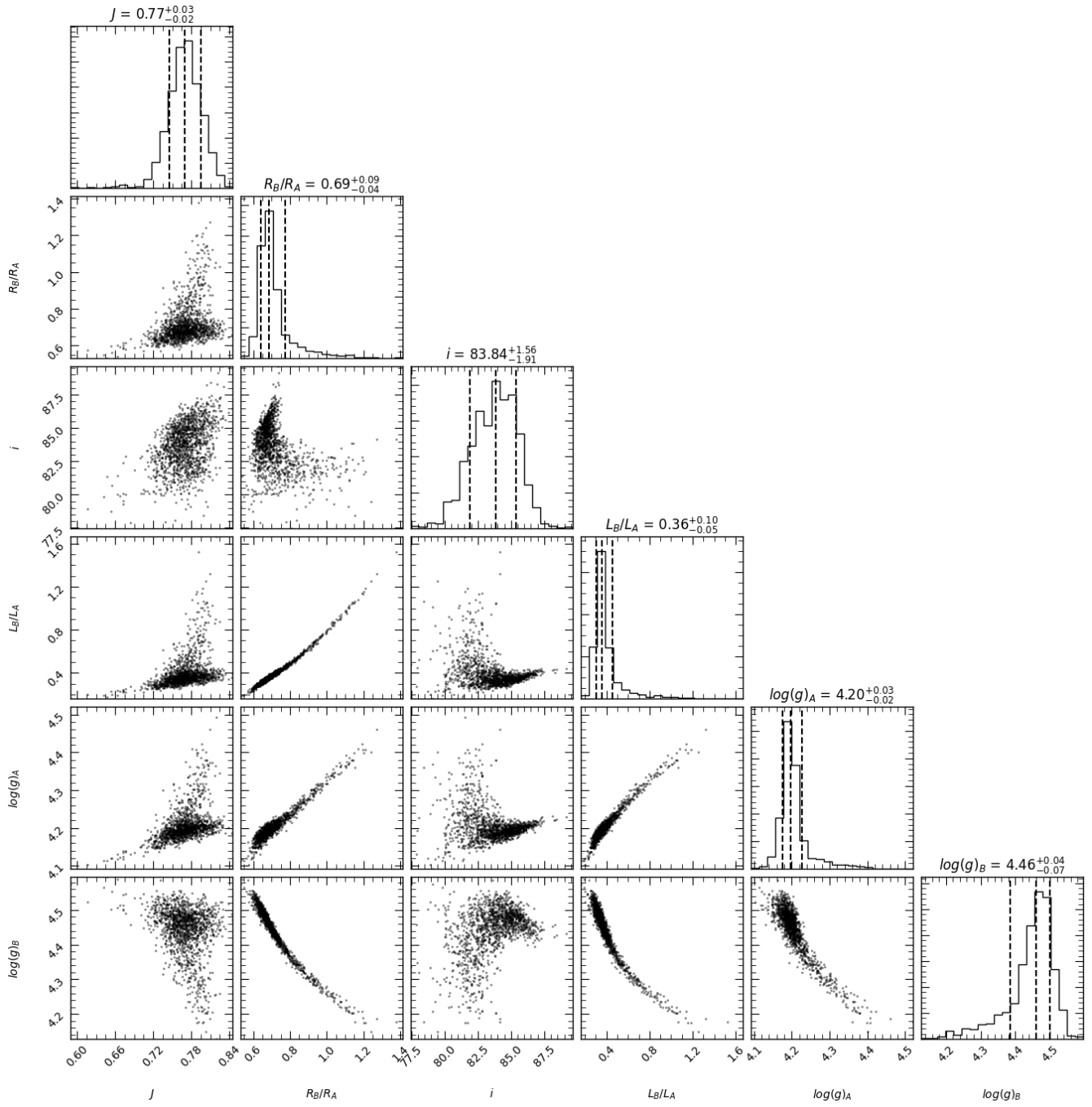


**Figure D3.** Corner plot for the residual-permutation simulations of ZTF *r* solution. Titles show 16, 50 and 84 percentiles.

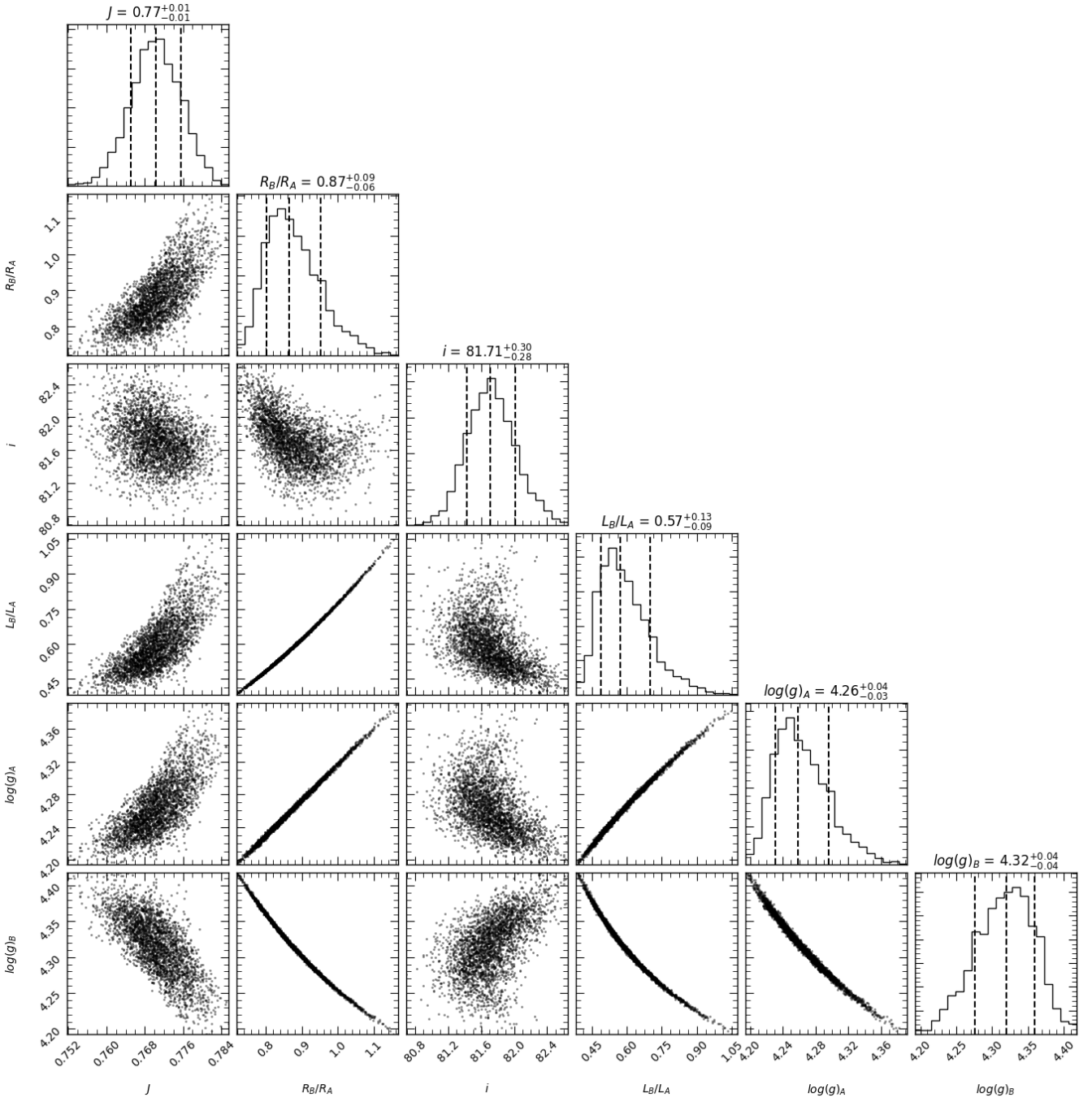


**Figure D4.** Corner plot for the residual-permutation simulations of TESS 44 solution. Titles show 16, 50 and 84 percentiles.

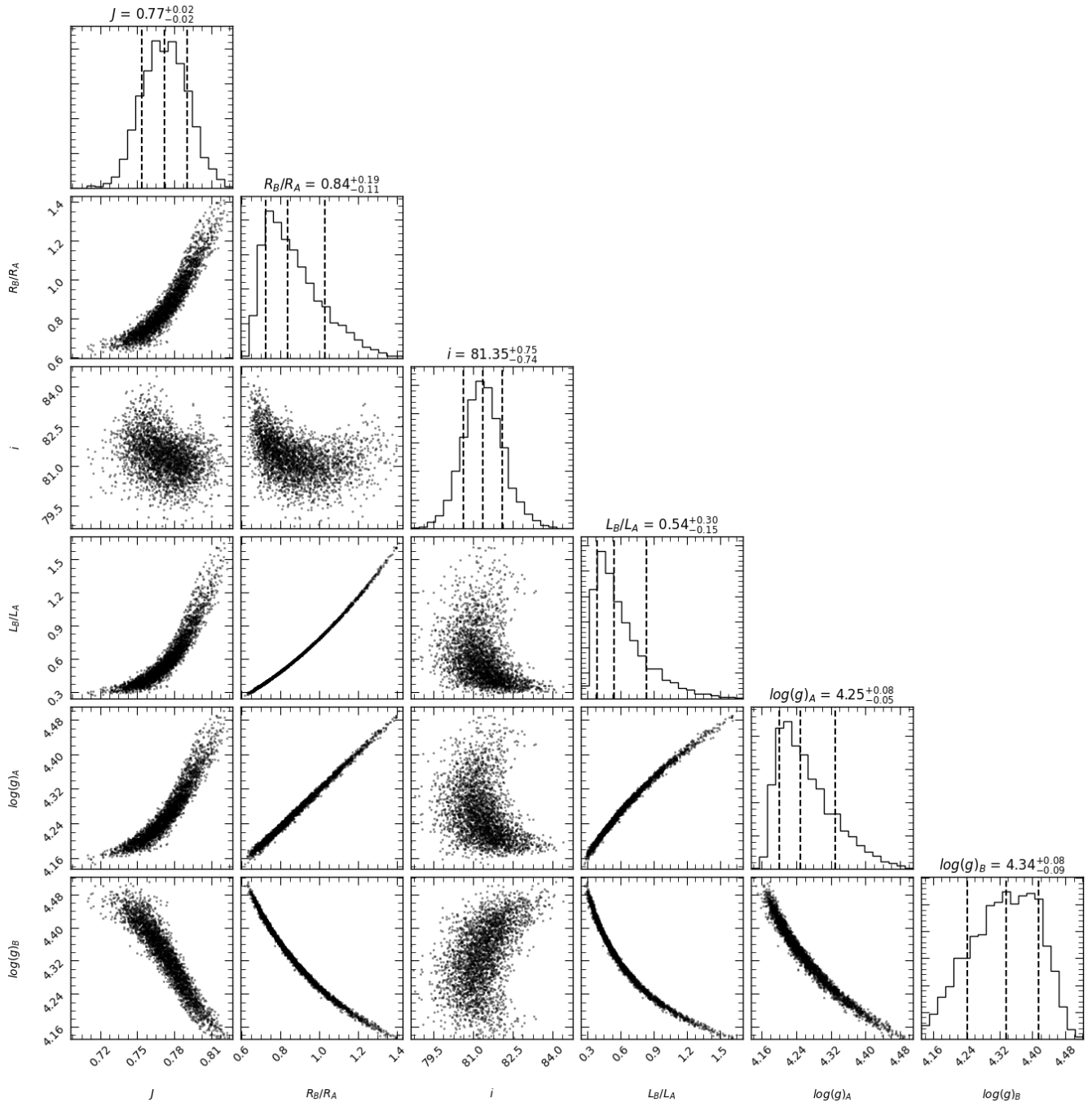


**Figure D5.** Corner plot for the residual-permutation simulations of TESS 45 solution. Titles show 16, 50 and 84 percentiles.



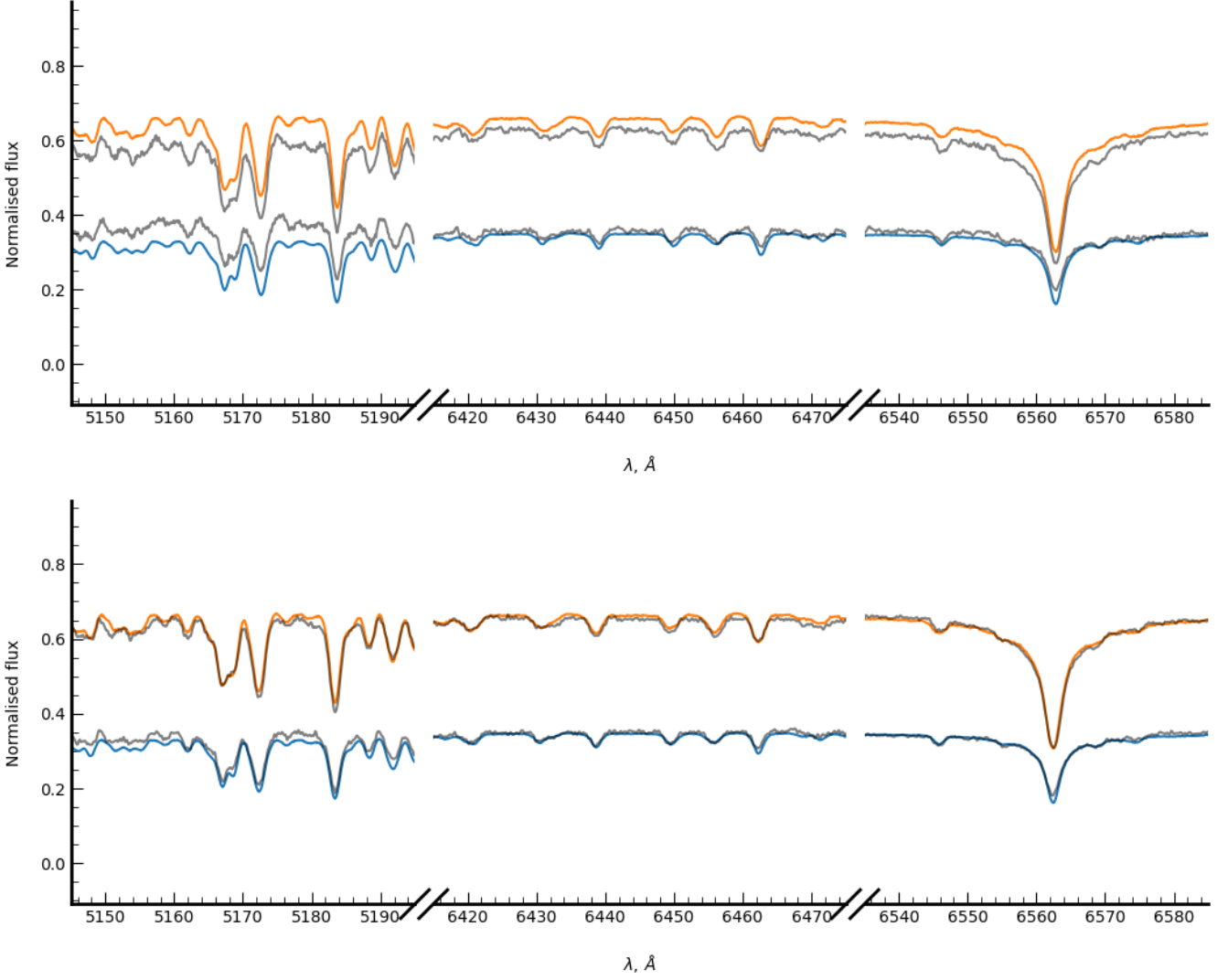


**Figure E1.** Comparison of the best-fit spectral models (blue and orange lines) with the separated spectra (gray lines) with offsets +0.15, -0.15 for primary and secondary. The top panel shows model for short epoch's spectra, fitted with the same [Fe/H] assumption and "shift and add" separation results. The bottom panel shows model for stacked spectra, fitted with the same [Fe/H] assumption and Fourier separation results. Note that Fourier separation spectra are blue-shifted according to  $\gamma$ .

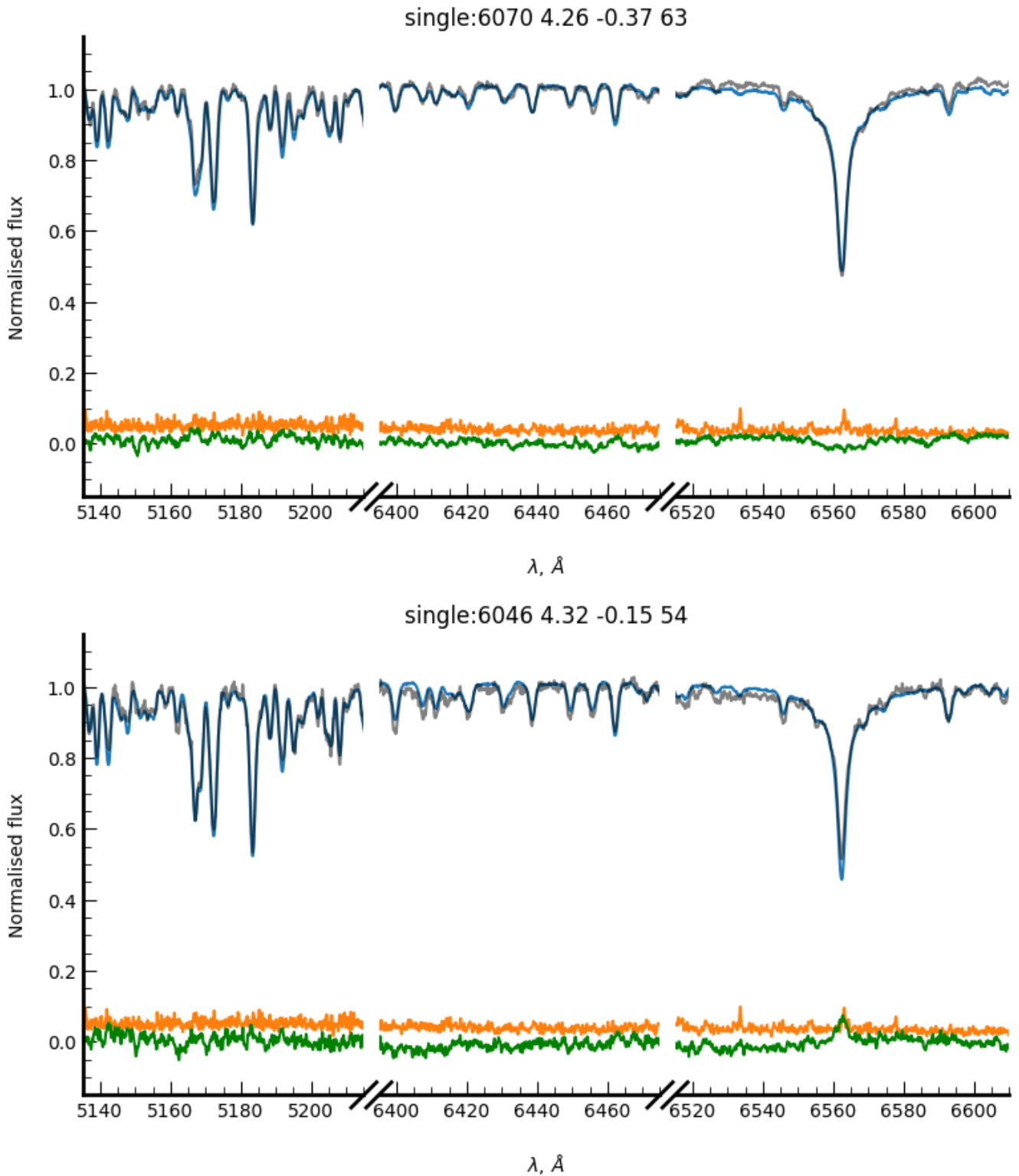


**Figure E2.** Separated spectra fitted by the single-star spectral model. The observed spectrum is shown as a gray line, the best fit is shown as blue line. The orange line is an error spectrum and the difference O-C is shown as a green line. The primary component is shown on the top panel, the secondary is shown on the bottom panel.

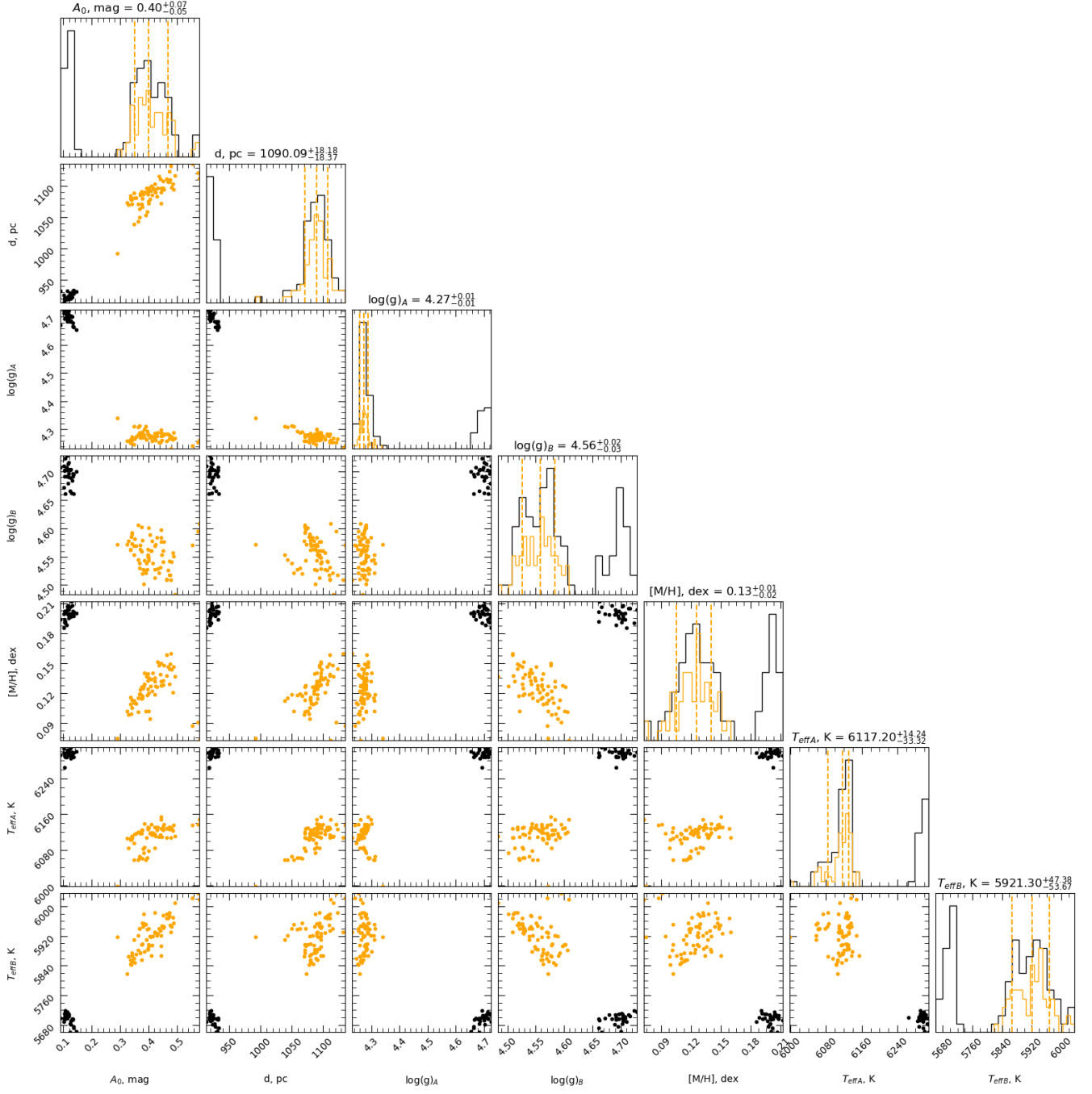


**Figure F1.** Corner plot for Gaia DR3 Multiple Star Classifier sample. Titles show 16, 50 and 84 percentiles for subsample with  $A_0 > 0.2$  mag.